

Numerical Investigation of Influential Factors in Hydraulic Fracturing Processes Using Coupled Discrete Element-Lattice Boltzmann Method

Weiwei Zhu¹, Zhiqiang Chen², Zhiguo Tian¹, and Moran Wang¹

¹Tsinghua University

²Petroleum Exploration and Production Research Institute, SINOPEC

February 27, 2023

Abstract

Hydraulic fracturing is widely used to stimulate unconventional reservoirs, but a systematic and comprehensive investigation into the hydraulic fracturing process is rare. In this work, a discrete element-lattice Boltzmann method is implemented to simulate the hydro-mechanical behavior in a hydraulic fracturing process. Different influential factors, including injection rates, fluid viscosity, in-situ stress states, heterogeneity of rock strengths, and formation permeability, are considered and their impacts on the initiation and propagation of hydraulic fractures are evaluated. All factors have a significant impact on fracture initiation pressure. A higher injection rate, higher viscosity, and larger in-situ stress increase the initiation pressure, while a higher formation permeability and higher heterogeneity decrease the initiation pressure. Injection rates and heterogeneity degrees have significant impacts on the complexity of generated fractures. Fluid viscosity, in-situ stress states, and formation permeability do not change the geometrical complexity significantly. Hydraulic fractures are usually tensile fractures, but many tensile fractures also have shear displacement. Shear fractures are possible and the shear displacement can be significant under certain conditions, such as a high injection rate, and a high heterogeneity degree.

Numerical Investigation of Influential Factors in Hydraulic Fracturing Processes Using Coupled Discrete Element-Lattice Boltzmann Method

Weiwei Zhu¹, Zhiqiang Chen², Zhiguo Tian¹, Moran Wang¹

¹Department of Engineering Mechanics, Tsinghua University, Beijing, China

²Petroleum Exploration and Production Research Institute, SINOPEC, Beijing, China

Key Points:

- Different influential factors have significant impacts on the initiation pressure.
- High injection rates and heterogeneity degrees increase the geometrical complexity of fractures.
- Hydraulic fractures are dominated by tensile fractures, but shear fractures are also possible.

Abstract

Hydraulic fracturing is widely used to stimulate unconventional reservoirs, but a systematic and comprehensive investigation into the hydraulic fracturing process is rare. In this work, a discrete element-lattice Boltzmann method is implemented to simulate the hydro-mechanical behavior in a hydraulic fracturing process. Different influential factors, including injection rates, fluid viscosity, in-situ stress states, heterogeneity of rock strengths, and formation permeability, are considered and their impacts on the initiation and propagation of hydraulic fractures are evaluated. All factors have a significant impact on the fracture initiation pressure. A higher injection rate, higher viscosity, and larger in-situ stress increase the initiation pressure, while a higher formation permeability and higher heterogeneity decrease the initiation pressure. Injection rates and heterogeneity degrees have significant impacts on the complexity of generated fractures. Fluid viscosity, in-situ stress states, and formation permeability do not change the geometrical complexity significantly. Hydraulic fractures are usually tensile fractures, but many tensile fractures also have shear displacement. Shear

Corresponding author: Moran Wang, mrwang@tsinghua.edu.cn

fractures are possible and the shear displacement can be significant under certain conditions, such as a high injection rate, and a high heterogeneity degree.

Plain Language Summary

Hydraulic fracturing technique is essential for the development of unconventional reserves, such as shale gas, shale oil, and geothermal reservoirs. To optimize hydraulic fracturing operations and enhance recovery efficiency, it is necessary to understand the process's mechanism and figure out the influential factors. Direct observations of the hydraulic fracturing process in the subsurface are impossible. In this work, we adopt a numerical scheme (DEM-LBM) to investigate the process in detail and consider as many factors as possible, including injection rates, fluid viscosity, in-situ stress states, heterogeneity of rock strengths, and formation permeability. The impacts of those influential factors on the initiation and propagation of hydraulic fractures are evaluated. We find that all factors have a significant impact on fracture initiation pressure. However, the complexity of generated fractures is mainly affected by injection rates and heterogeneity degrees of rock strengths. Generated hydraulic fractures are usually tensile fractures, but shear fractures are possible and the shear displacement can be significant under certain conditions, such as a high injection rate, and a high heterogeneity degree. Continued research is required to further include the interactions between factors and it is completely possible with the foundation constructed in this work.

1 Introduction

Hydraulic fracturing refers to the process of injecting highly-pressurized liquid into a well to break up bedrock formations, which is vastly implemented in stimulating unconventional reservoirs, e.g. shale oil, shale gas, and enhanced geothermal systems (Pruess, 2006; Gandossi & Von Estorff, 2013).

The hydraulic fracture process is quite complex and cannot be observed directly in the deep subsurface. Microseismicity techniques are effective to locate fracture events and distinguish failure modes but cannot provide detailed information on fracture initiation and propagation (N. Warpinski et al., 2004; H. Chen et al., 2018). Therefore, many lab experiments and numerical simulations are conducted to investigate the hydraulic fracturing process. Experiments under triaxial and true triaxial stress conditions are widely adopted to mimic the actual geostress states (Huang & Liu, 2017; X. Zhao et al., 2019). The

58 acoustic emission method is used to monitor the hydraulic fracturing process (Stanchits
59 et al., 2014; Goodfellow et al., 2015), but similar to the microseismicity method in the
60 field, detailed morphology information of fractures is not available. To observe the fracture
61 morphologies inside rock samples, Liu et al. (2018) experimentally investigated the hydraulic
62 fracturing process in heterogeneous samples under different stress anisotropy levels and the
63 morphological patterns of hydraulic fractures are identified with CT scanning. Similar
64 methods are adopted by Yushi et al. (2016), Kumari et al. (2018), and many others. CT
65 scanning method is limited to the resolution and long operation time, which is difficult to
66 capture the real-time variations of fracture initiation and propagation process. In addition,
67 hydraulic fracturing experiments are destructive experiments, which means the samples are
68 not reusable after fracking. 3D-printed samples can reproduce the same rock samples and
69 optical visualization is available (Liu et al., 2016), but the printing materials are usually
70 far different from actual rocks in terms of physical and mechanical properties. Also, having
71 a comprehensive investigation of the influential factors requires a large number of rock
72 samples, which is both time-consuming and financially expensive.

73 Numerical simulation of the hydraulic fracturing process is a useful way to conduct
74 sensitivity analysis of influential factors. The hydraulic fracturing process is a strongly cou-
75 pled hydro-mechanical process. For the mechanical part, several continuum and mesoscale
76 numerical methods are used to simulate fracture initiation and propagation. The continuum
77 methods mainly include the boundary element method (Olson & Taleghani, 2009; Cheng et
78 al., 2022), extended finite element method (XFEM) (Dahi-Taleghani & Olson, 2011; Mo-
79 hammadnejad & Khoei, 2013), and phase field methods (Wilson & Landis, 2016; Heider,
80 2021). However, the continuum method usually involves high requirements for mesh quality
81 and complicated treatments for complex boundary conditions. Therefore, the mesoscale
82 numerical method is also widely used to simulate mechanical deformation, which mainly
83 refers to the discrete element method (DEM). DEM directly describes the mechanical dis-
84 placements and interactions of discontinues particles (Cundall & Strack, 1979). For the
85 fluid dynamics part, the assumption of lubrication flow is usually used since a fracture
86 has a width significantly smaller than its length. The finite volume method (FVM) and
87 finite element method (FEM) can be used to discretize and solve the flow equations and
88 couple with mechanical part (Peirce & Detournay, 2009; Lecampion, 2009; Wangen, 2011;
89 Papachristos et al., 2017). However, the lattice Boltzmann method (LBM) has several ad-
90 vantages compared with FVM and FEM, such as simple calculation procedures, convenient

91 implementation of parallel computation, and simple treatment of complex geometries. In
92 addition, through the Chapman-Enskog theory, the Navier-Stokes equations can be derived
93 from the Boltzmann equation (S. Chen & Doolen, 1998). Therefore, the LBM method can
94 solve the Navier-Stokes equations and overcome the possible inaccuracy caused by the lu-
95 brication flow assumption. Coupled DEM-LBM method is a good option for simulating the
96 hydro-mechanical coupling process (S. A. Galindo-Torres et al., 2012; S. Galindo-Torres,
97 2013; Z. Chen & Wang, 2017; Z. Chen et al., 2020).

98 Many factors can influence the geometry of hydraulic fractures, like formation parame-
99 ters (e.g. in-situ stress), treatment parameters (e.g. injection rate and fluid viscosity), and
100 rock properties (e.g. rock strength heterogeneity and formation permeability). Zeng and
101 Roegiers (2002); De Pater and Beugelsdijk (2005); Liu et al. (2018); Zhuang et al. (2019);
102 Fazio et al. (2021) and Y. Zhao et al. (2022) investigated the impact of injection rate, fluid
103 viscosity, stress states, and matrix permeability on the hydraulic fracturing process with
104 lab experiments. The results provide helpful insights, but lab experiments cannot use an
105 identical rock sample in each test. A strict factor control leads to a large number of indi-
106 vidual experiments and lab experiments usually cannot exclude the impact of intrinsic rock
107 characteristics, such as the heterogeneity of natural rocks. In contrast, numerical simula-
108 tions can have better factor controls and investigate the impact of each factor. Nagaso et
109 al. (2015); Wang et al. (2016); Z. Chen et al. (2020) and Duan et al. (2018) investigated
110 the impact of fluid viscosity, injection rate, and in-situ states on the fracture propagation
111 process through different numerical methods. However, a comprehensive investigation of
112 the hydraulic fracturing process considering all the influential factors mentioned above is
113 rare (Zhuang & Zang, 2021). In this work, we aim to have a comprehensive investigation
114 considering the impacts of injection rate, fluid viscosity, heterogeneity of rock strength, for-
115 mation permeability, and in-situ stress state on the initiation and propagation of hydraulic
116 fractures, which is helpful to deepen the understanding of hydraulic fracturing processes.

117 In this work, a DEM-LBM method is adopted to simulate the hydraulic fracturing
118 process, and Section. 2 introduces detailed information about the coupled method. Impacts
119 of different factors on fracture initiation and propagation are demonstrated in Section. 3. In
120 Section. 4, we discuss the limitation of the method and possible improvements. Important
121 conclusions are summarized in Section. 5.

2 Methods and materials

2.1 A DEM-LBM scheme for the simulation of hydraulic fracturing process

A DEM-LBM method is adopted in this work to simulate the coupled hydro-mechanical process. The numerical framework is based on the multi-physics simulation software MECHSYS developed by S. Galindo-Torres (2013) and extension of the software developed by Z. Chen and Wang (2017) and Z. Chen et al. (2018, 2020). Only a brief introduction of the method is covered in this section and more detailed information is available in the references above.

DEM treats materials as an assembly of discrete particles. In this work, the interactions between particles are approximated with linear contact and bonding models. In the linear contact model, the contact can happen between different geometrical patterns of two particles, including edge-edge and vertex-face for polyhedrons (S. A. Galindo-Torres et al., 2012). The normal elastic force \vec{F}_n^c between different geometrical pairs (P_i and P_j) is given by:

$$\vec{F}_n^c(P_i, P_j) = K_n \vec{\delta}(P_i, P_j), \quad (1)$$

Where K_n is the normal contact stiffness, $\vec{\delta}(P_i, P_j)$ is the normal displacement (overlapping) vector between a geometric pattern pair. The net elastic force is the summation of forces for all pairs of geometrical patterns.

Similarly, the tangential contact force \vec{F}_t^c is given by:

$$\vec{F}_t^c = K_t \vec{\zeta}(P_i, P_j), \quad (2)$$

where K_t is the tangential contact stiffness and $\vec{\zeta}(P_i, P_j)$ is the tangential displacement vector between a geometric pattern pair.

In the bonding model, two neighboring spheropolyhedra sharing a common face are connected with an elastic force. The cohesive force in the normal direction \vec{F}_n^b is given by:

$$\vec{F}_n^b = B_n A \vec{\epsilon}_n, \quad (3)$$

where B_n is the normal elastic modulus of the material, A is the shared face area between particles, and $\vec{\epsilon}_n$ is the normal strain in the direction normal to the common face and positive for tensile deformation. The normal cohesive force is calculated for tensile deformation only and Eq. 1 accounts for the normal elastic force in a compressive deformation.

148 The cohesive force in the tangential direction \vec{F}_t^b is given by:

$$\vec{F}_t^b = B_t A \vec{\epsilon}_t, \quad (4)$$

149 where B_t is the tangential elastic modulus of the material, and $\vec{\epsilon}_t$ is the shear strain in the
150 direction tangential to the common face.

151 A threshold value on the total strain, denoted as ϵ_{th} , is provided as the criterion of
152 fracture initiation:

$$|\vec{\epsilon}_n| + |\vec{\epsilon}_t| \geq \epsilon_{th}, \quad (5)$$

153 where $\vec{\epsilon}_n$ and $\vec{\epsilon}_t$ are the normal and tangential strain caused by the displacement of adjacent
154 faces.

155 A broken bond is classified as a shear failure if its shear strain is larger than the normal
156 strain. Similarly, a tensile failure refers to a case where the tensile strain is larger than the
157 shear strain. A similar classification is adopted in Shimizu et al. (2011) and Z. Chen and
158 Wang (2017).

159 The lattice Boltzmann method (LBM) is a useful computational fluid dynamics method
160 for fluid simulation, where the fluid is regarded as fictive particles, and the density distri-
161 bution functions of particles are simulated through streaming and collision processes. In
162 this work, a D3Q15 model is chosen to simulate the fluid flow considering the accuracy and
163 computation efficiency. The corresponding evolution equation is:

$$f_i(\vec{x} + \vec{e}_i \delta t, t + \delta t) = f_i(\vec{x}, t) - \frac{\delta t}{\tau} (f_i(\vec{x}, t) - f_i^{eq}(\vec{x}, t)), \quad i = 0, 1, 2 \dots 14, \quad (6)$$

164 where f_i and f_i^{eq} are the density distribution function and the corresponding equilibrium
165 distribution in the i th discrete velocity direction, \vec{e}_i , δt is the time step adopted in the
166 simulation, and τ is the relaxation time. Through the Chapman-Enskog analysis, the fluid
167 kinematic shear viscosity ν is related to τ by:

$$\nu = \frac{1}{3} c^2 \left(\tau - \frac{\delta t}{2} \right), \quad (7)$$

168 where c is the lattice speed in LBM. Note that all parameters in lattice Boltzmann equations
169 are dimensionless with "lattice units". To map the lattice units to physical units, proper
170 conversion factors are required. A set of basic conversion factors, composed of time, length,
171 and mass, is sufficient to derive the dimension of any physical parameters in this work. The
172 corresponding basic conversion factors are C_l , C_t , and C_ρ , since the length, time and density

173 are natural quantities in LB simulations.

$$C_l = \frac{\delta x^*}{\delta x} \quad (8)$$

$$C_t = \frac{\delta t^*}{\delta t} \quad (9)$$

$$C_\rho = \frac{\rho^*}{\rho} \quad (10)$$

176 Note that the parameters with * have physical units. δx and δt are the grid size and time
 177 step used in the simulation. Usually, δx and δt are 1 in LBM implementation and we use
 178 the physical density as the lattice density. Therefore, the corresponding conversion factors
 179 are $C_l = \delta x^*$, $C_t = \delta t^*$, and $C_\rho = 1$. The conversion factor for ν can be obtained through a
 180 simple dimension analysis:

$$C_\nu = \frac{C_l^2}{C_t} \quad (11)$$

181 Therefore, the physical kinematic viscosity of the simulated fluid is

$$\nu^* = \frac{1}{3} \left(\tau - \frac{1}{2} \right) \frac{\delta^2 x^*}{\delta t^*} \quad (12)$$

182 The fluid density and velocity can be obtained from the density distribution function:

$$\rho = \sum_i f_i \quad (13)$$

$$\vec{u} = \frac{\sum_i f_i \vec{e}_i}{\rho} \quad (14)$$

184 The pressure can also be obtained from the Chapman-Enskog analysis:

$$p = \frac{1}{3} \rho c^2 \quad (15)$$

185 In the fluid simulation, we care more about the pressure difference concerning the initial
 186 pressure instead of the specific pressure. Therefore, with a proper conversion factor, the
 187 physical pressure difference can be calculated by:

$$\Delta p^* = \frac{1}{3} \Delta \rho \frac{\delta^2 x^*}{\delta^2 t^*} \quad (16)$$

188 An immersed boundary method (IBM) is applied to incorporate the fluid-solid inter-
 189 actions (Noble & Torczynski, 1998; Z. Chen & Wang, 2017). The basic logic behind the
 190 IBM method is that the fluid flow is simulated in the whole domain including the particles.
 191 For fluid inside a particle, a body force is inserted to make the fluid have the same rigid
 192 movement as the particle and the no-slip boundary condition is fulfilled for the external fluid
 193 flow. A fluid-solid interaction term Ω_i^{fs} is added in the standard LBM evolution equation.

$$f_i(\vec{x} + \vec{e}_i \delta t, t + \delta t) = f_i(\vec{x}, t) + (1 - B) \left\{ -\frac{\delta t}{\tau} (f_i - f_i^{eq}) \right\} + B \Omega_i^{fs}, \quad (17)$$

194 where B is a weighting parameter, which is a function of τ and the solid volume fraction γ :

$$B = \frac{\gamma(\tau/\delta t - 1/2)}{(1 - \gamma) + (\tau/\delta t - 1/2)}, \quad (18)$$

195 where γ is defined as the ratio of the solid volume over the lattice volume. When $\gamma = 0$, there
 196 are no solids in the corresponding fluid lattice. When $\gamma = 1$, the lattice is fully occupied
 197 by the solid phase. When $B = 0$, corresponding to $\gamma = 0$ (fluid lattice), the evolution
 198 equation degenerates to the standard one. Ω_i^{fs} can be obtained from a "bounce-back" of
 199 the nonequilibrium part of the density distribution:

$$\Omega_i^{fs} = f_{-i}(\vec{x}, t) - f_i(\vec{x}, t) + f_i^{eq}(\rho, \vec{u}_s) - f_{-i}^{eq}(\rho, \vec{u}_s), \quad (19)$$

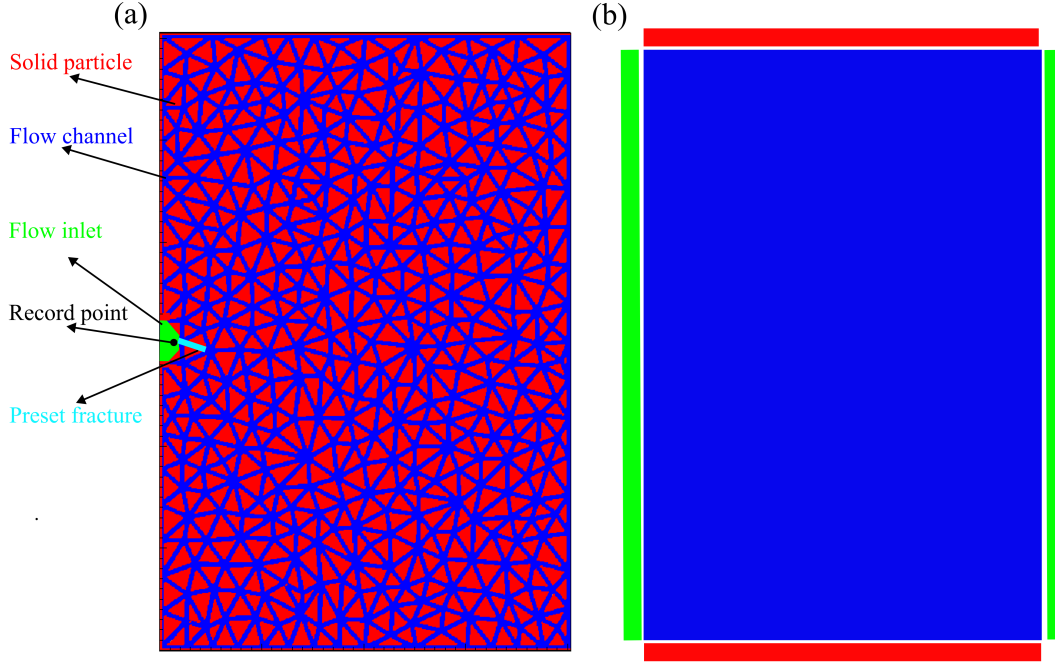
200 where f_{-i} refers to the "bounce-back" state from f_i by reversing all unit velocity vector,
 201 i.e. \vec{e}_i to $-\vec{e}_i$, and u_s is the velocity of the solid particle at time $t + \delta t$ at the position
 202 \vec{x} . To obtain the solid velocity, a force analysis of the particle is required. However, in
 203 this work, the particles are assumed to be unmovable to avoid the numerical error caused
 204 by particle vibrations. For cases with non-negligible particle velocities, Z. Chen and Wang
 205 (2020) proposed an improved IBM method, which incorporates the inertial force term with
 206 a finite-difference expression.

207 In Appendix A and Appendix B, a gravity-driven Poiseuille flow in a slit and a Brazilian
 208 test are used to validate the correctness of LBM and DEM schemes.

209 2.2 Simulation setup

213 The simulation model considered is a rectangular plate with a width of 4.0 cm, length
 214 of 6.0 cm, and thickness of 1.28 mm. The solid particles are shown in red in Fig. 1(a) with
 215 a total number of 741. The solid particles are eroded and dilated to form channels for the
 216 fluid flow (shown in blue in Fig. 1). The solid volume fraction γ is used to control the initial
 217 permeability of the flow domain in the LBM lattice. For the whole flow domain, there is a
 218 predefined γ controlling the initial permeability of the matrix, which can be used to mimic
 219 the leakage of injected fluid to formation in reality. A small cave on the left side is assigned
 220 as the fluid inlet and the initial γ value is zero. A preset fracture is denoted in Fig. 1(a),
 221 which mimics the perforation process in reality and helps to intrigue the hydraulic fracture.
 222 The detailed simulation parameters are listed in Table. 1.

223 Four rectangular plates on each side of the domain are added to implement differ-
 224 ent stresses on the horizontal (left-right) and vertical (top-bottom) directions, shown in



210 **Figure 1.** Calculation domain with a length of 6 cm, a width of 4 cm, and a thickness of 1.28
 211 mm

225 Fig. 1(b). The horizontal and vertical plates have a length of 4.0×10^{-2} m and 6.0×10^{-2}
 226 m. The width and height of plates are the same as the thickness of the particle, 1.28×10^{-3}
 227 m. There is a constant flow-rate condition for the inlet and a fixed pressure is assigned on
 228 the right side of the domain. All the other boundaries are set as solid.

229 Since the discrete element method is only conditionally stable, the time step should
 230 be small enough to reach the convergence. The critical time step is a function of the
 231 particle mass, its stiffness, and its arrangement (O’Sullivan & Bray, 2004). To ensure the
 232 convergence, the time step fulfills the criterion below (S. A. Galindo-Torres et al., 2012):

$$\Delta t_{critical} = 0.1 \sqrt{\frac{M_{min}}{C_{nmax} + B_{nmax}}}, \quad (20)$$

233 where M_{min} is the minimum mass of all particles, C_{nmax} and B_{nmax} are the maximum
 234 normal contact and bond stiffness of all particles, respectively. From Eq. 20, a larger value
 235 of the particle stiffness, a smaller time step is required. In this work, the heterogeneity of
 236 rock strengths is considered, which focuses more on the variations of rock strengths. Specific
 237 rock strengths are excluded as the influential factor. Therefore, we reduce the stiffness and
 238 modulus values to increase the time step as shown in Table. 1, which makes the simulation
 239 computationally affordable (Yousefi & Ng, 2017).

212

Table 1. Input parameters for the DEM-LBM simulation

| Parameter | Value |
|-------------------------------------|--|
| Normal contact stiffness, K_n | 1.0×10^6 N/m |
| Tangential contact stiffness, K_t | 1.0×10^6 N/m |
| Normal elastic modulus, B_n | 2.0×10^6 [Pa] |
| Tangential elastic modulus, B_t | 4.2×10^6 [Pa] |
| Bond strength, ϵ_{th} | 0.01 [-] |
| Fluid density, ρ_f^* | 1.0×10^3 [kg/m ³] |
| Lattice size in LBM, δ_x^* | 1.0×10^{-4} [m] |
| Time step in DEM/LBM, δ_t^* | 1.0×10^{-6} [s] |

240 If the bond strengths of all particles are the same, it will lead to a homogeneous rock
 241 sample. However, real rock samples are always heterogeneous because of different mineral
 242 compositions and cement materials. Therefore, the heterogeneous bond strengths are more
 243 appropriate for real rocks and it is one of the influential factors investigated in this work.
 244 The Weibull distribution is widely adopted to describe heterogeneous bond strengths for
 245 brittle rocks (Van Mier et al., 2002; Z. Chen & Wang, 2017; Pan et al., 2018; Z. Chen et
 246 al., 2020):

$$f(\epsilon_{th}) = \frac{m}{\epsilon_{th}^0} \left(\frac{\epsilon_{th}}{\epsilon_{th}^0}\right)^{m-1} \exp\left(-\left(\frac{\epsilon_{th}}{\epsilon_{th}^0}\right)^m\right), \quad (21)$$

247 where ϵ_{th}^0 is the average bond strength threshold and is set as 0.01 in this work. m is the
 248 shape parameter, describing the heterogeneity degree of the bond strength. An infinitely
 249 large m corresponds to a homogeneous structure, while a low value of m indicates a hetero-
 250 geneous structure.

251 The influential parameters investigated in this work also include the injection rate
 252 and in-situ stress states. To properly choose the injection rate and the stress levels, we
 253 conducted a Buckingham analysis (Buckingham, 1915) with the following steps and scaled
 254 our simulation parameters with parameters in actual experiments.

- 255 • Choose possible variables: tensile strength S , viscosity of fluid ν , particle size l ,
 256 injection rate q , fluid density ρ . In total, the number of variables is 5;
- 257 • Find variables with repeating units: particle size l , injection rate q , fluid density
 258 ρ . Therefore, the number of dimensions is 3 and the basis of fundamental units are

259 T (time), L (distance), and M (mass). Therefore, there should be two independent
 260 dimensionless parameters (π_1 and π_2) concerning fluid viscosity ν and tensile strength
 261 S .

- 262 • The first dimensionless parameter π_1 :

$$\pi_1 = \nu \times l^a \times q^b \times \rho^c \quad (22)$$

263 The unit of π_1 is:

$$[\pi_1] = \left[\frac{L^2}{T}\right] \times [L]^a \times \left[\frac{L^3}{T}\right]^b \times \left[\frac{M}{L^3}\right]^c \quad (23)$$

264 Since π_1 is dimensionless, we have:

$$\pi_1 = \frac{\nu \cdot l}{q}, \quad (24)$$

265 which is similar to the Reynolds number, if l is the characteristic length of the flow
 266 channel.

- 267 • The second dimensionless parameter π_2 :

$$\pi_2 = S \times l^a \times q^b \times \rho^c \quad (25)$$

268 The unit of π_2 is:

$$[\pi_2] = \left[\frac{M}{T^2 L}\right] \times [L]^a \times \left[\frac{L^3}{T}\right]^b \times \left[\frac{M}{L^3}\right]^c \quad (26)$$

269 Since π_2 is dimensionless, we have:

$$\pi_2 = \frac{Sl^4}{q^2 \rho} = \frac{S}{\rho q^2 / l^4}, \quad (27)$$

270 where the denominator part is equivalent to the dynamic pressure term $\frac{1}{2}\rho u^2$.

271 To estimate proper injection rates and stress levels, we take the experiment parameters
 272 from Liu et al. (2018), i.e. $q = 3.26 \times 10^{-7} \text{ m}^3/\text{s}$, $\nu = 6.7 \times 10^{-5} \text{ m}^2/\text{s}$, $S = 5.7 \times 10^6 \text{ Pa}$,
 273 and $\rho = 1000 \text{ kg/m}^3$. The particle size l is estimated as $5.0 \times 10^{-3} \text{ m}$ for the glutenite
 274 rock used in the experiment. On the simulation side, we choose the dynamic viscosity
 275 as $\nu_s = 5.0 \times 10^{-4} \text{ m}^2/\text{s}$ and fluid density as $\rho_s = 1000 \text{ kg/m}^3$. The particle size is esti-
 276 mated by $l_s = 0.25\sqrt{A_{\max}}$, where $A_{\max} = 5.0 \times 10^{-6} \text{ m}^2$ is the maximum particle area in
 277 the simulation. Correspondingly, the injection rate in the simulation is estimated from π_1 ,
 278 $q_s = 2.72 \times 10^{-7} \text{ m}^3/\text{s}$, and the corresponding injection velocity is $u_s = 0.34 \text{ m/s}$. From
 279 π_2 , the proper magnitude of tensile strength can be estimated. Please note that the tensile
 280 strength in the simulation should be scaled according to the elastic modulus and failure
 281 criterion. As a result, a stress magnitude of 10 MPa in the experiment corresponds to

282 1.68×10^4 Pa in the simulation. In this way, proper values of injection rates and stress
 283 levels are found for the simulation with an appropriate magnitude.

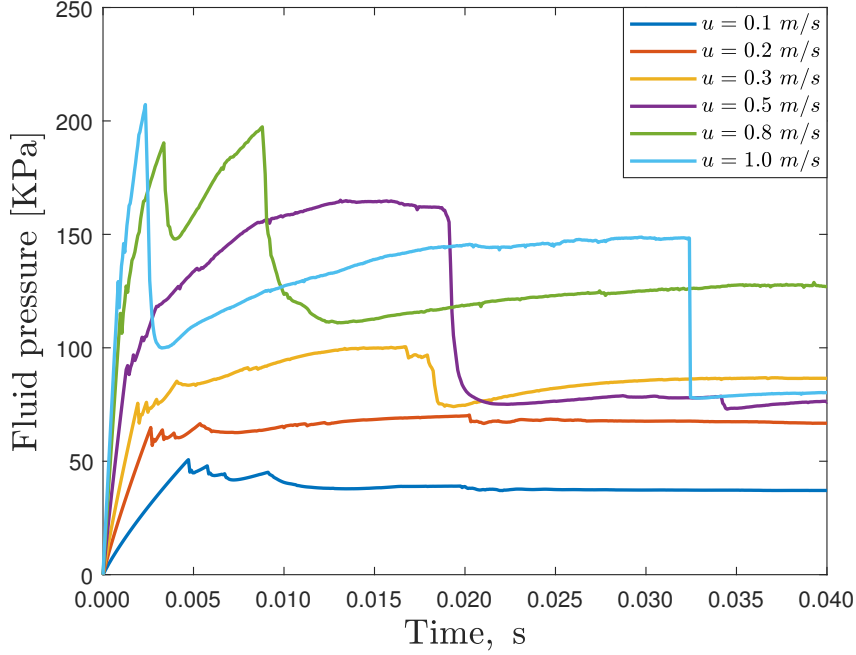
284 **3 Results**

285 We systematically investigate the individual impact of injection rates, fluid viscosity,
 286 in-situ stresses, heterogeneous bond strengths, and formation permeability on fracture ini-
 287 tiation and propagation. Each influential factor is evaluated with the other factors fixed at
 288 a reference value. The reference value for each parameter is listed as follows: 0.2 m/s for
 289 the injection velocity, 5.0×10^{-4} m²/s for the fluid kinematic viscosity, no stress state for
 290 the in-situ stress states, homogeneous bond strengths for heterogeneous bond strengths and
 291 a solid volume fraction of 0.97 for the formation permeability.

292 **3.1 Impact of injection rate**

293 Six different injection velocities are chosen for the investigation under an unconfined
 294 condition: 0.1 m/s, 0.2 m/s, 0.3 m/s, 0.5 m/s, 0.8 m/s and 1.0 m/s. The pore pressure
 295 variations of the inlet position (the record point shown in Fig. 1a) are shown in Fig. 2.
 296 With injection velocity increases, the fracture initiation pressure also increases, consistent
 297 with many observations from lab experiments and numerical simulation (Morgan et al., 2017;
 298 Zhuang et al., 2019; Duan et al., 2018). For low injection velocities ($u = 0.1$ and 0.2 m/s),
 299 the pore pressure vibrates, but decreases with fracture propagation, which indicates that
 300 the fracture volume and leak-off volume expand at a roughly equal or a slightly greater
 301 rate than the injection rate. For high injection velocities ($u > 0.2$ m/s), the pore pressure
 302 continues to increase after the fracture initiation, indicating that the fracture volume and
 303 leak-off volume increase at a smaller rate than the injection rate.
 304

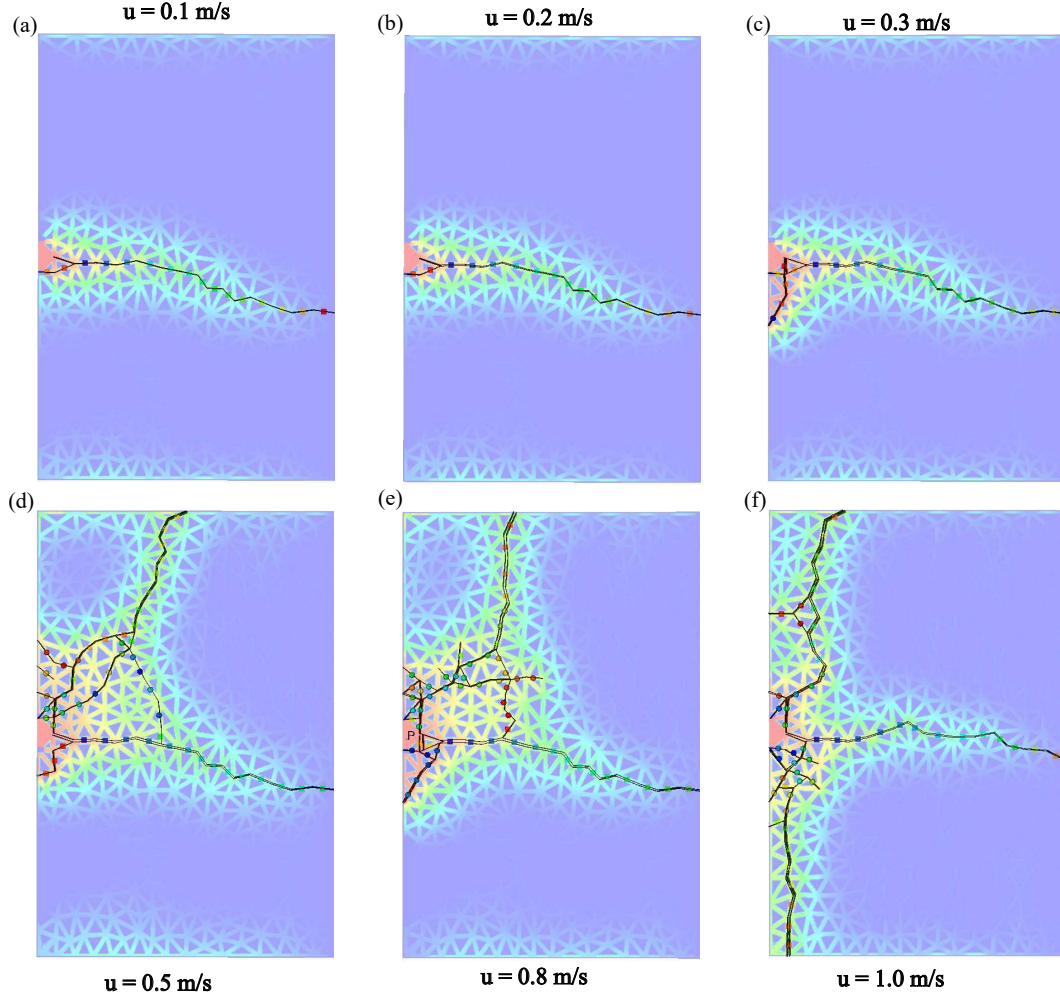
305 The fracture geometries of each case are shown in Fig. 3 with the fluid pressure dis-
 306 tribution shown in the background. The center point of each fracture is represented by a
 307 solid square for a tensile fracture and a circle for a shear fracture. The color variations from
 308 cold (blue) to warm (red) refer to the sequence of generation. For low injection velocity,
 309 the fracture geometries are almost the same (Fig. 3(a,b)). However, with the increasing
 310 injection velocities, the fracture geometries become complex with branches. The main hori-
 311 zontal fractures in different cases are similar. However, when the horizontal fracture reaches
 312 the right boundary, vertical fractures tend to form at a high injection velocity and most
 313
 314
 315
 316



293 **Figure 2.** The pore pressure evolution at the record point for cases with different injection rates

317 fractures generated in the transition zones (from horizontal to vertical) are shear instead
 318 of tensile fractures. When the horizontal fracture reaches the right boundary, the pore
 319 pressure in the hydraulic fracture compresses the sample in the top-bottom direction. The
 320 stress condition makes the newly generated fracture perpendicular to the horizontal fracture
 321 because the fracture trace should be perpendicular to the minimum principle stress (zero
 322 stress in the left-right direction). In addition, when the injection velocity is high, the pore
 323 pressure becomes significantly high as shown in Fig. 2, which is large enough to generate a
 324 new fracture in the top-bottom direction.

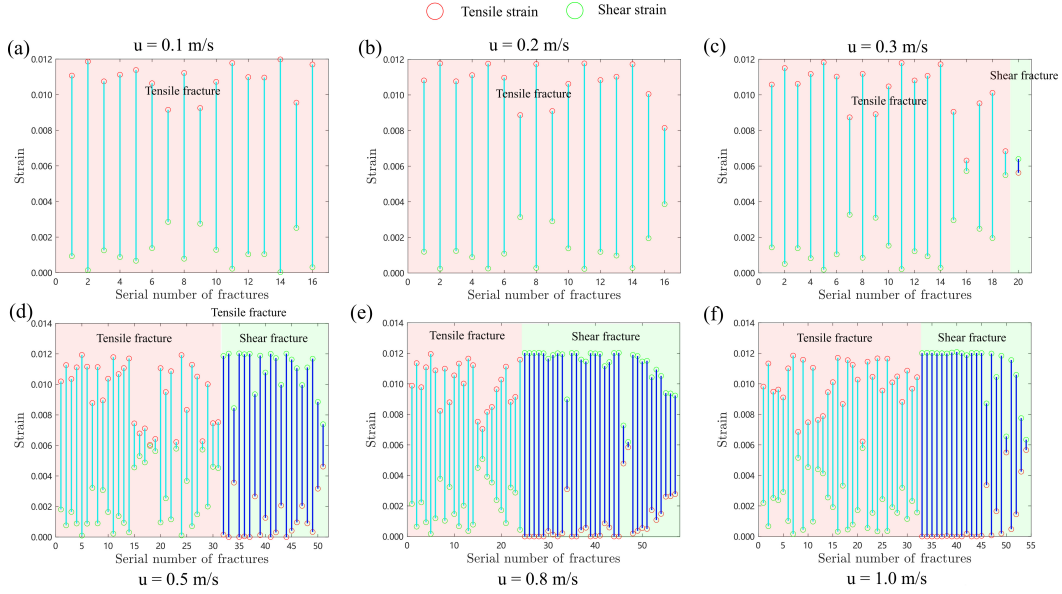
326 Fig. 4 shows the tensile and shear strain component of each fracture segment in Fig. 3.
 327 The tensile and shear strains are represented with red and green circles, respectively. The
 328 links between tensile and shear strain for tensile and shear fractures are light blue and
 329 regular blue. When the injection rate is small, all fractures are tensile fractures with in-
 330 significant shear strain between particles. However, when the injection rate increases, more
 331 fractures have a comparable even larger shear strain than tensile strain. The proportion of
 332 shear fractures increases with the increasing injection velocity, which is consistent with the
 333 observation in Duan et al. (2018).



305 **Figure 3.** Fracture geometries of cases with different injection rates at 0.04s. The background
 306 shows the fluid pressure distribution in the entire domain. The center of each fracture segment is
 307 marked with squares for tensile fractures and circles for shear fractures. The color variations from
 308 blue to red refer to the generation sequence of each type of fractures.

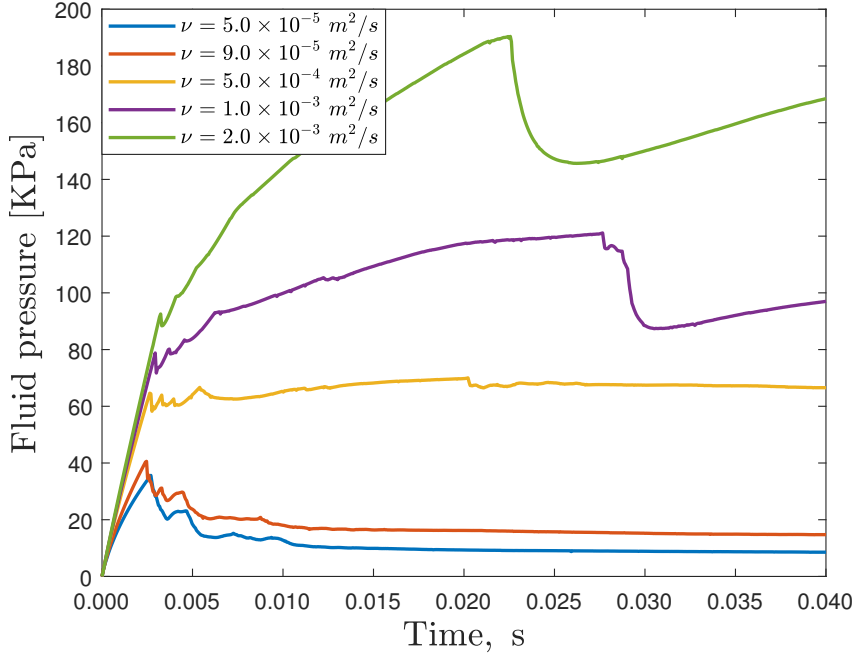
334 3.2 Impact of fluid viscosity

340 Six levels of viscosity are chosen for the investigation under an unconfined condition:
 341 $\nu = 5.0 \times 10^{-5} \text{ m}^2/\text{s}$, $9.0 \times 10^{-5} \text{ m}^2/\text{s}$, $2.0 \times 10^{-4} \text{ m}^2/\text{s}$, $5.0 \times 10^{-4} \text{ m}^2/\text{s}$, $1.0 \times 10^{-3} \text{ m}^2/\text{s}$,
 342 $2.0 \times 10^{-3} \text{ m}^2/\text{s}$. The pore pressure variations at the record point are shown in Fig 5. With
 343 viscosity increases, the initial stage of the pressure build-up of all cases is similar, but the
 344 initiation pressure increases for the case with a high viscosity. Similar results are observed
 345 in Duan et al. (2018) and Z. Chen et al. (2020). The fracture geometries are similar for
 346 different fluid viscosity and three examples are presented in Fig. 6. When the viscosity is



325

Figure 4. Tensile and shear strain of each fracture segment in Fig. 3



335

Figure 5. The pore pressure evolution at the record point for cases with different fluid viscosity

347

low, the fluid can leak into the formation easily and make the pore pressure of the formation

348

increase as shown in Fig.6(a). Also, a few branches along the main hydraulic fracture can be

349

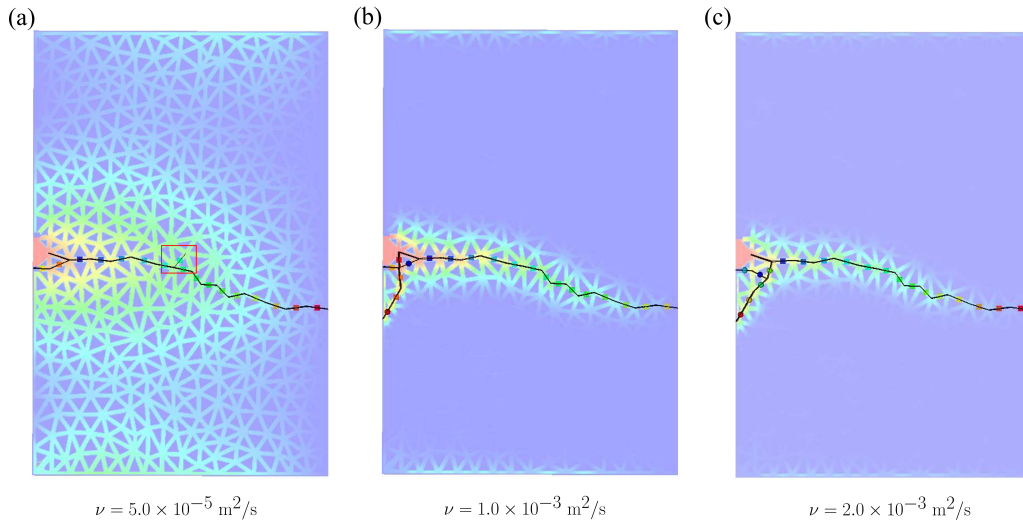
observed in Fig. 6(a). For high-viscosity fluid, the pore pressure can only propagate to the

350

neighboring region and the region area shrinks with increasing viscosity. In addition, after

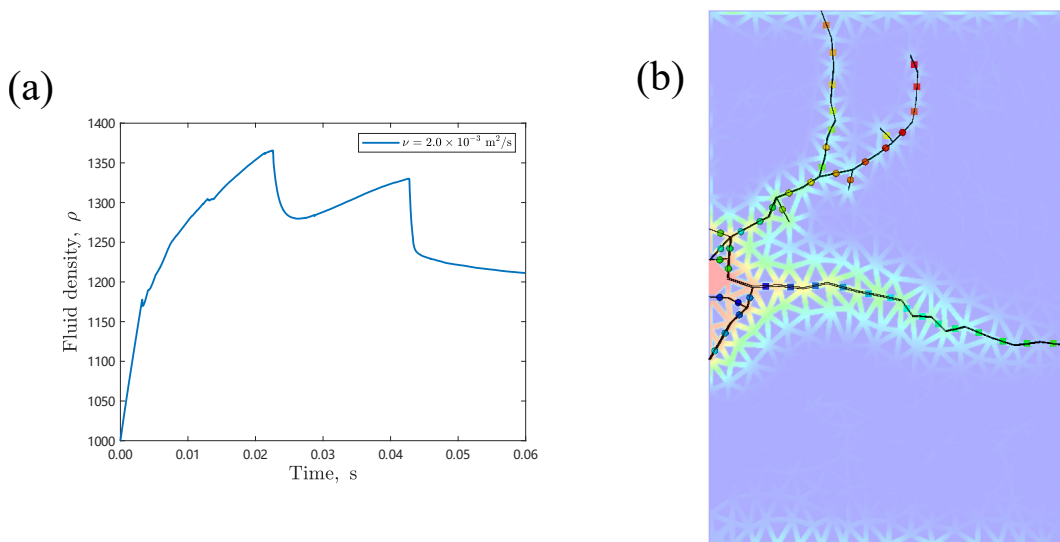
351

the horizontal fracture reaches the right boundary, new fractures can be generated at the



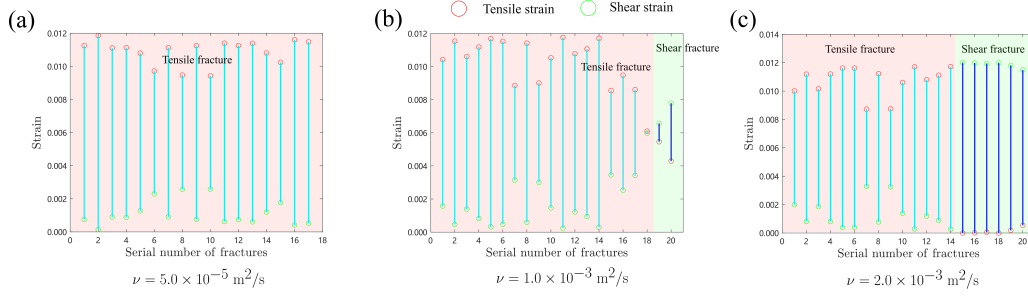
336 **Figure 6.** Fracture geometries of cases with different fluid viscosity at 0.04s. A branch generated
 337 in the low-viscosity case is marked in the red box.

352 inlet because of the high pore pressure therein as shown in Fig. 5. For the highest viscosity
 353 considered in this work, $\nu = 2.0 \times 10^{-3} \text{ m}^2/\text{s}$, the pore pressure continues to increase after
 354 0.04 s as shown in Fig. 7(a). New fractures are generated in the vertical direction and
 355 continue to propagate as shown in Fig. 7(b). Most inclined fractures are shear fractures and
 the fractures become tensile in a perpendicular direction.



338 **Figure 7.** The pore pressure evolution at the record point for cases with high fluid viscosity,
 339 $\nu = 2.0 \times 10^{-3} \text{ m}^2/\text{s}$ (a) and the corresponding fracture geometries (b) at 0.06s.

357 Fig. 8 presents the strain component of each fracture segment in Fig. 6. When the
 358 viscosity is low, all generated fractures are tensile fractures. With the increasing viscosity,
 359 the shear strain becomes more significant and the proportion of shear fractures also increases.
 360 However, the main horizontal fractures are mostly tensile and shear fractures are usually
 the newly generated inclined fractures.



356 **Figure 8.** Tensile and shear strain of each fracture segment in Fig. 6

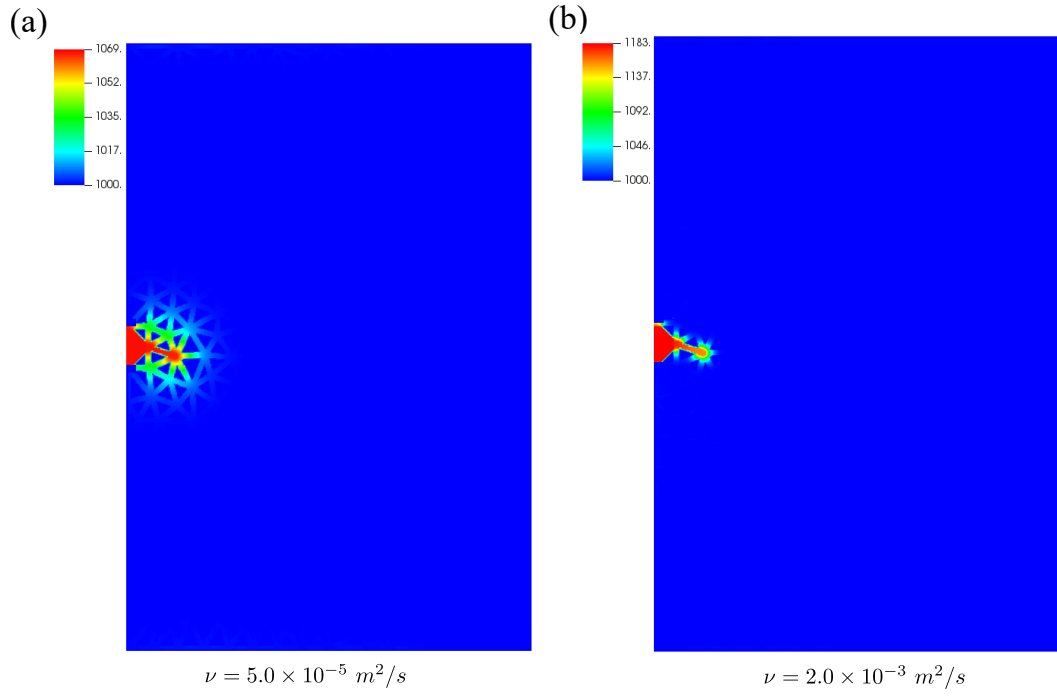
361

362 Fluid with low viscosity has stronger penetration capability than highly viscous fluid.
 363 Fig. 9 shows the pressure distribution of cases with low and high fluid viscosity at the fracture
 364 initiation stage. The pressure propagates much farther in the low-viscosity case. Similar
 365 observations are obtained from Duan et al. (2018) and Z. Chen et al. (2020). The penetration
 366 capability may not change the fracture geometries significantly in the homogeneous media
 367 since all bonds are equally strong. However, for heterogeneous media or formations with
 368 preexisting natural fractures, such penetration capability can help to generate more complex
 369 fracture geometries (Z. Chen et al., 2020).

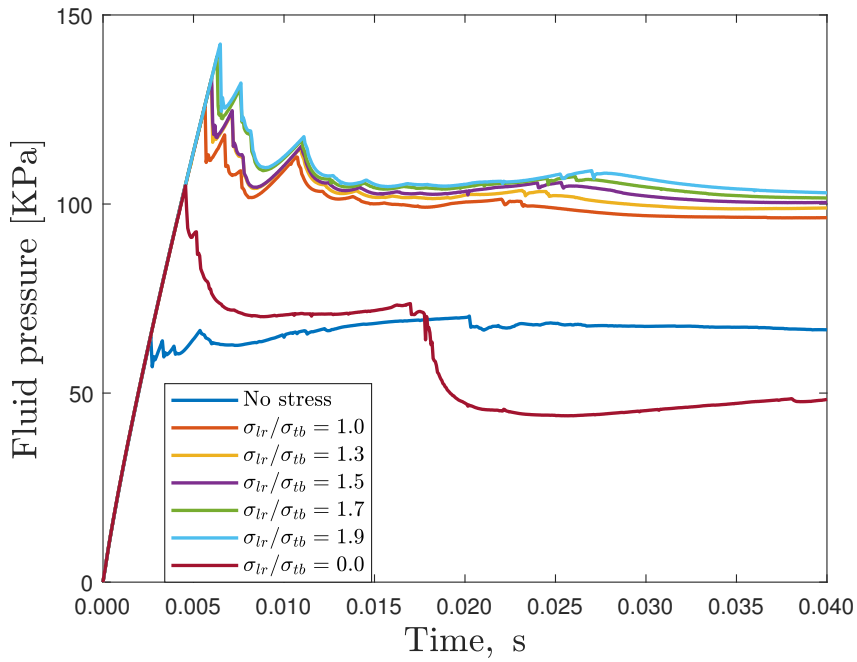
372 3.3 Impact of in-situ stress states

373 The stress on the top-bottom direction is fixed at 1.68×10^4 Pa as derived in Section. 2.
 374 Different stress anisotropy degrees are represented by the stress ratio between σ_{lr} (left-
 375 right direction) and σ_{tb} (top-bottom direction). Six levels of the ratio are chosen for the
 376 investigation: $\sigma_{lr}/\sigma_{tb} = 1.0, 1.3, 1.5, 1.7, 1.9, 0$.

380 The pore pressure variations of each case at the record point are shown in Fig. 10,
 381 where the initiation pressure increases due to the imposed in-situ stresses. A larger imposed
 382 in-situ stress leads to a higher fracture initiation pressure. However, the implementation of

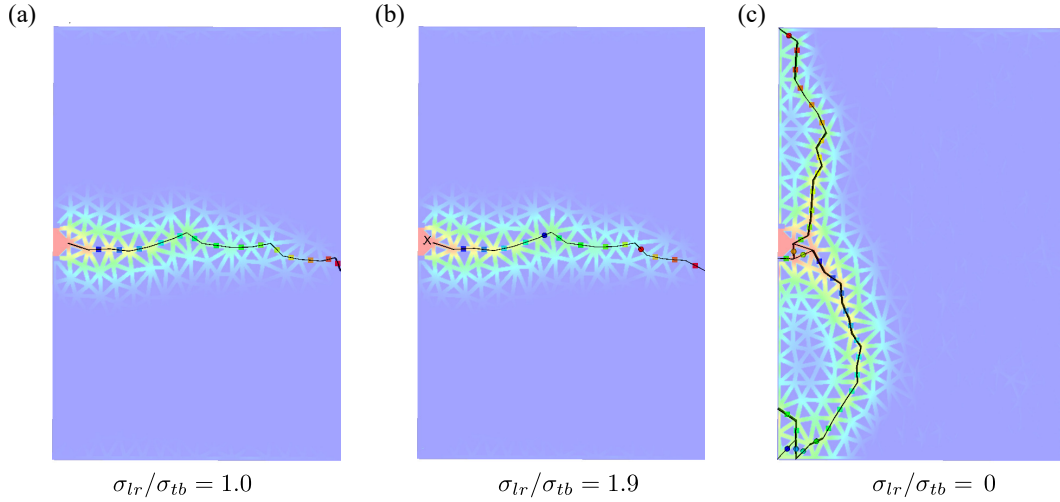


370 **Figure 9.** Pore pressure distribution at the fracture initiation stage for cases with a low(a) and
 371 high (b) fluid viscosity, respectively



377 **Figure 10.** The pore pressure evolution at the record point for cases with different in-situ stress
 378 states

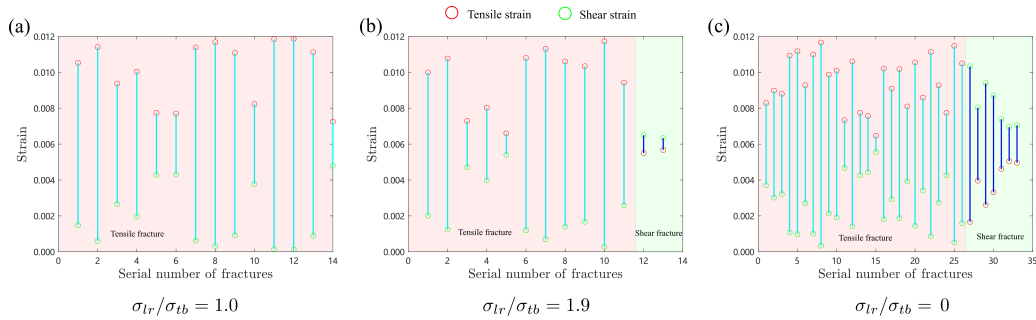
383 in-situ stress does not change the fracture geometry significantly. For the first five cases,
 384 where σ_{lr} is the maximum principle stress, the fracture geometries are similar and have
 385 a direction perpendicular to the minimum stress direction (top-bottom direction). Two
 386 examples of with $\sigma_{lr}/\sigma_{tb} = 1.0$ and 1.9 as shown in Fig. 11(a and b). For the case where no
 387 stress applies in the left-right direction, the fracture propagates in the top-bottom direction
 388 as expected, which is perpendicular to the minimum principle stress (left-right direction has
 no stress).



379 **Figure 11.** Fracture geometries of cases with different in-situ stress states at 0.04s

389

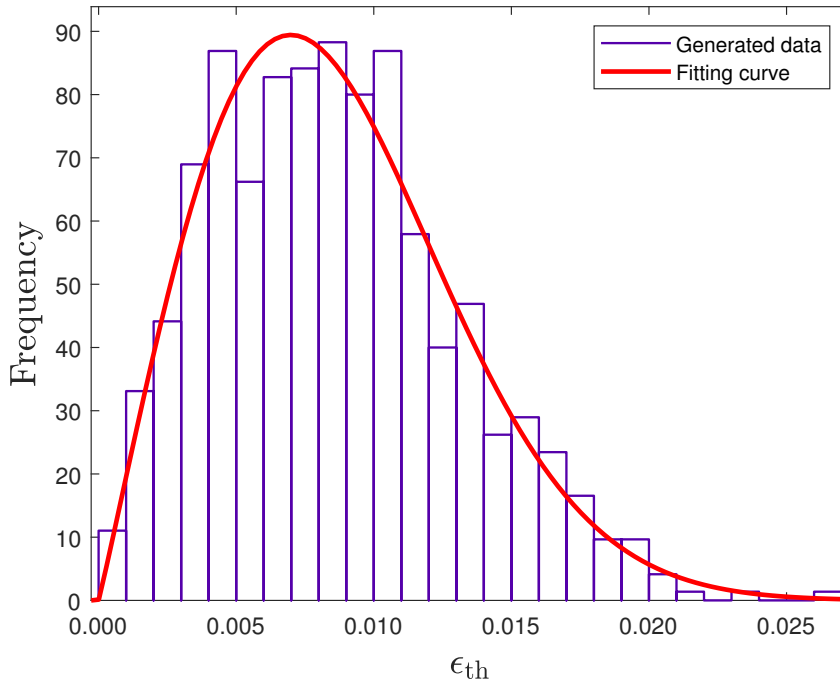
391 Fig. 12 shows the tensile and shear strain of each generated fracture in Fig. 11. The
 392 fractures are dominated by tensile fractures, but the shear fractures tend to increase with
 393 the anisotropy level. In addition, compared with the cases with no stress imposed (Fig. 4a),
 several tensile fractures have significant shear strain components.



390 **Figure 12.** Tensile and shear strain of each fracture segment in Fig. 11

394 **3.4 Impact of heterogeneous bond strengths**

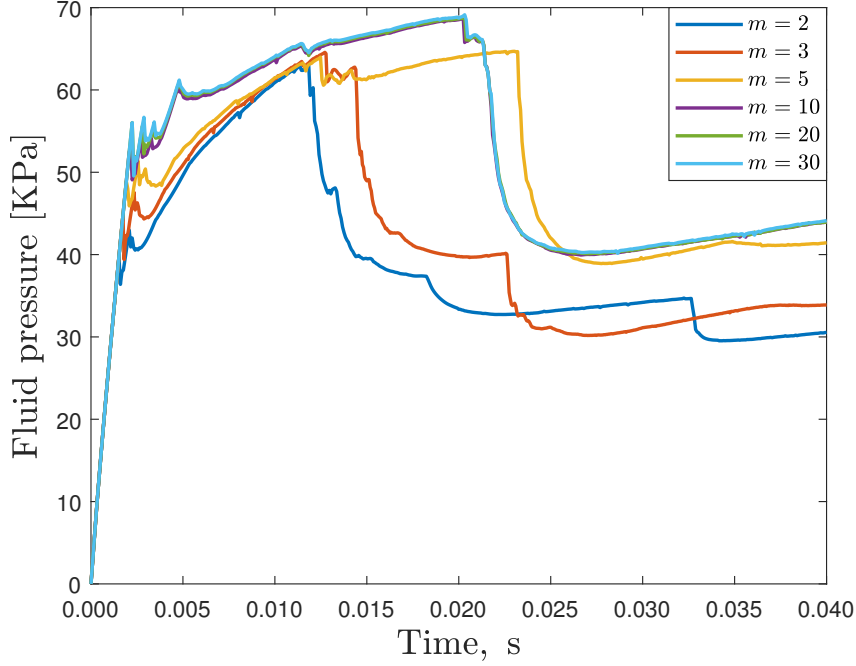
396 To investigate the heterogeneous characteristic of natural rocks, we choose different
 397 values of m in the Weibull distribution to make the bond strength vary. The average bond
 398 strength is 0.01 and six values of m are chosen for the consideration: $m = 2, 3, 5, 10, 20, 30$,
 399 A smaller m value represents a higher heterogeneity degree. For the case with $m = 2$, the
 400 strength distribution and the fitting curve are shown in Fig. 13. The fitting parameters are
 401 0.0097 for the mean and 2.04 for the shape factor, m . Therefore, the chosen quantity of
 402 particles (741) is sufficient to recover the prescribed distribution for the heterogeneous bond
 strengths.



395 **Figure 13.** A Weibull distribution fitting of heterogeneous bond strengths

403

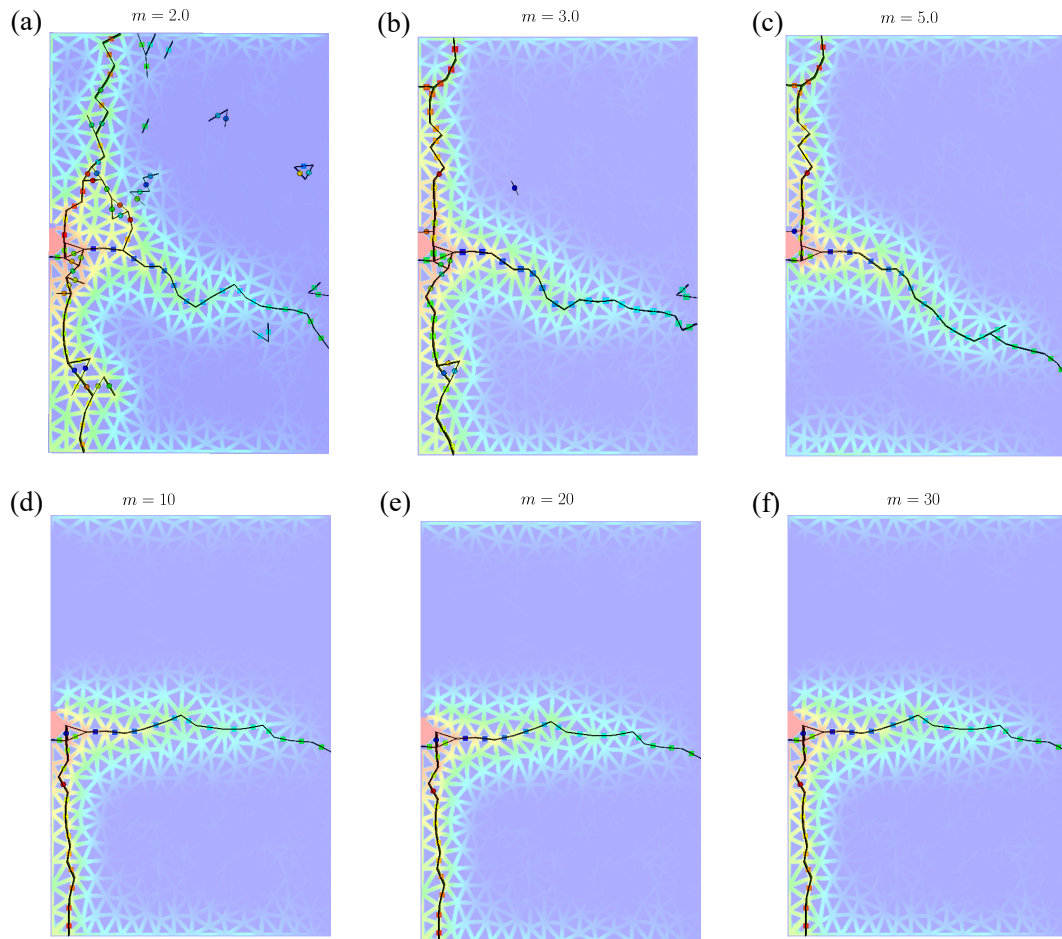
406 The pore pressure variations of each case at the record point are shown in Fig. 14. The
 407 pressure buildup process is the same for all cases with different heterogeneity. However, the
 408 initiation pressure is higher for cases with more homogeneous levels. The most heterogeneous
 409 case, where $m = 2.0$, has the lowest initiation pressure.



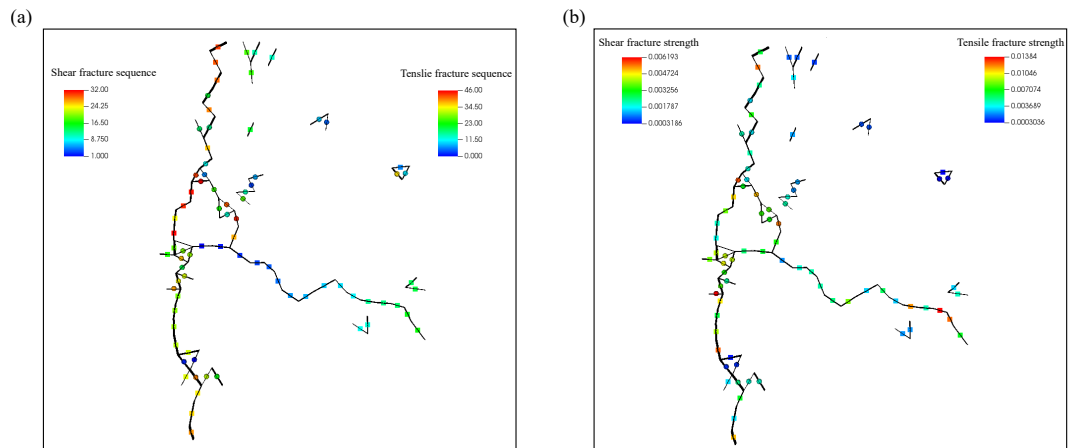
404 **Figure 14.** The pore pressure evolution at the record point for cases with different heterogeneity
 405 degrees of bond strengths

412 The fracture geometries of each case are shown in Fig. 15. The higher the heterogeneity
 413 degree is, the more complex the fracture geometry is. For the case with $m = 2.0$, the frac-
 414 ture geometries are the most complex with several branches. There are also some fractures
 415 disconnected from the main fractures, which are caused by the leakage of fluid into the
 416 matrix. To better demonstrate this process, the fracture traces are plotted with the bond
 417 strength and generation sequence marked in Fig. 16. Most disconnected fractures are shear
 418 fractures and their bond strengths are quite low as shown in Fig. 16(b). For the disconnected
 419 fractures, the leakage of injected fluid can enhance the pore pressure therein and the high
 420 pressure in the main hydraulic fracture can increase the local principal stresses. The in-
 421 creased principal stresses usually stifle possible microseismicity from occurring as concluded
 422 in N. R. Warpinski et al. (2001) and Zhu et al. (2022). However, there are no initial stresses
 423 applied in this simulation, therefore, the increase of principle stresses and pore pressure can
 424 trigger the shear failure or even tensile failure of those weak bonds.

428 For more homogeneous cases, where m is large, the fracture geometries do not change
 429 significantly. However, compared with a completely homogeneous case (Fig. 3a), there are
 430 two main fracture traces instead of a single horizontal one. This fracture geometry is similar

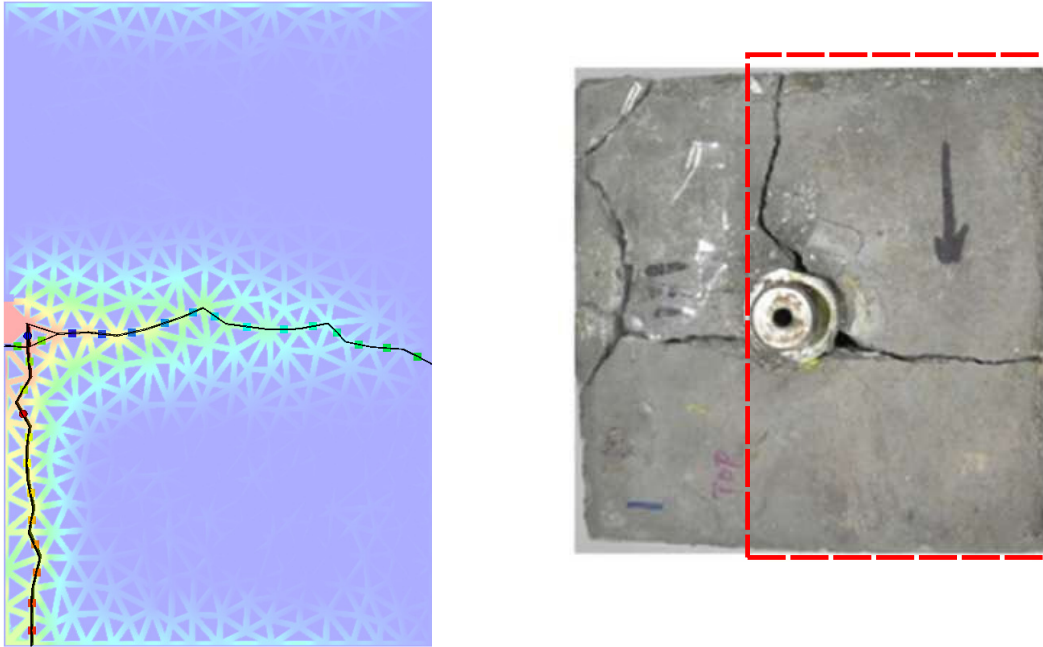


410 **Figure 15.** Fracture geometries of cases with different heterogeneity degrees of bond strengths
 411 at 0.04s



425 **Figure 16.** The generation sequence (a) and bond strength (b) of each fracture segment

431 to the experiment results in Liu et al. (2018) as shown in Fig. 17 since the actual rocks are
 432 not completely homogeneous. Similar patterns do support the correctness of the numerical
 method in this work.



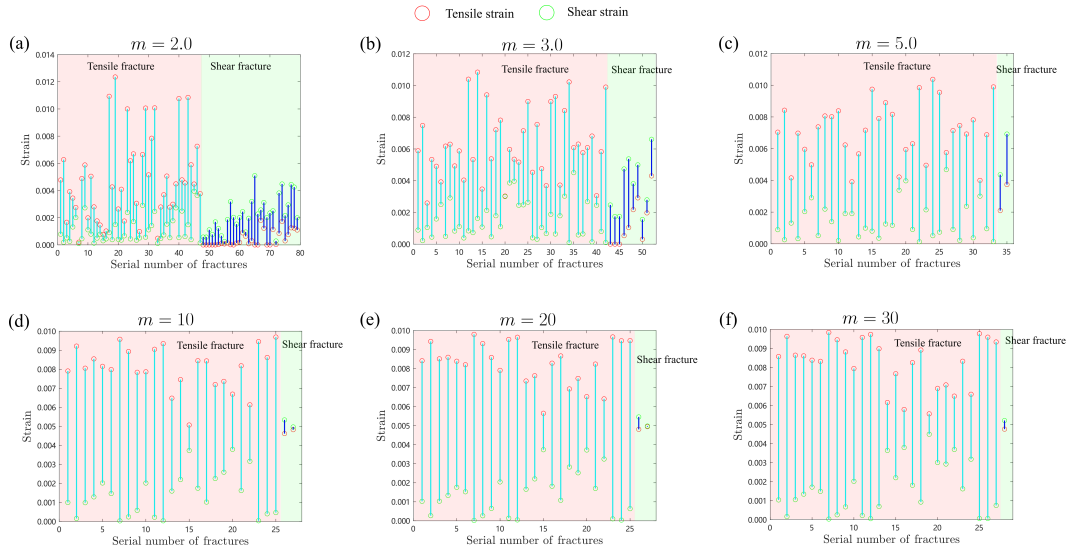
426 **Figure 17.** A comparison of fracture geometries with results in a lab experiment (Liu et al.,
 427 2016)

433

434 The strain components of each fracture in Fig. 15 are shown in Fig. 18. For highly
 435 heterogeneous cases, many shear fractures are generated. For the most heterogeneous case,
 436 32 out of 78 fractures are shear fractures, corresponding to a proportion of 41%. With
 437 the heterogeneity degree decreases, the proportion of shear fractures decreases sharply and
 438 tensile fractures are dominated.

440 **3.5 Impact of formation permeability**

441 The solid volume fraction (γ) has a negative correlation with the formation perme-
 442 ability. A larger γ indicates that more voids are occupied by impermeable solids and the
 443 corresponding formation permeability is lower. Impacts of different values of solid volume
 444 fractions (γ) are evaluated and six values are chosen: $\gamma = 0.85, 0.9, 0.92, 0.95, 0.97, 0.99$.

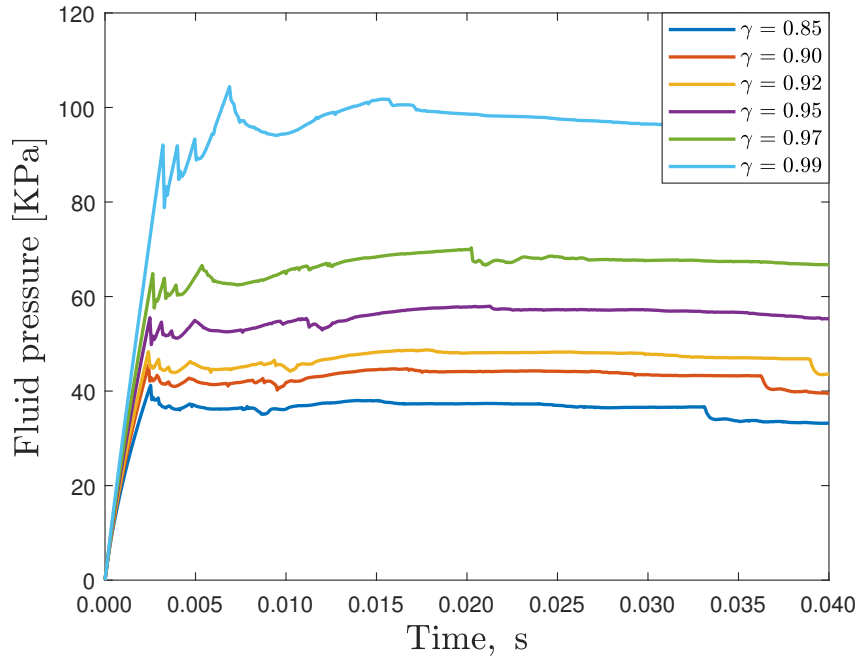


439

Figure 18. Tensile and shear strain of each fracture segment in Fig. 15

448

The pore pressure variations at the record point for different cases are shown in Fig. 19. The pressure evolution curves have similar shapes. The lower the matrix permeability, the



445

Figure 19. The pore pressure evolution at the record point for cases with different matrix permeability

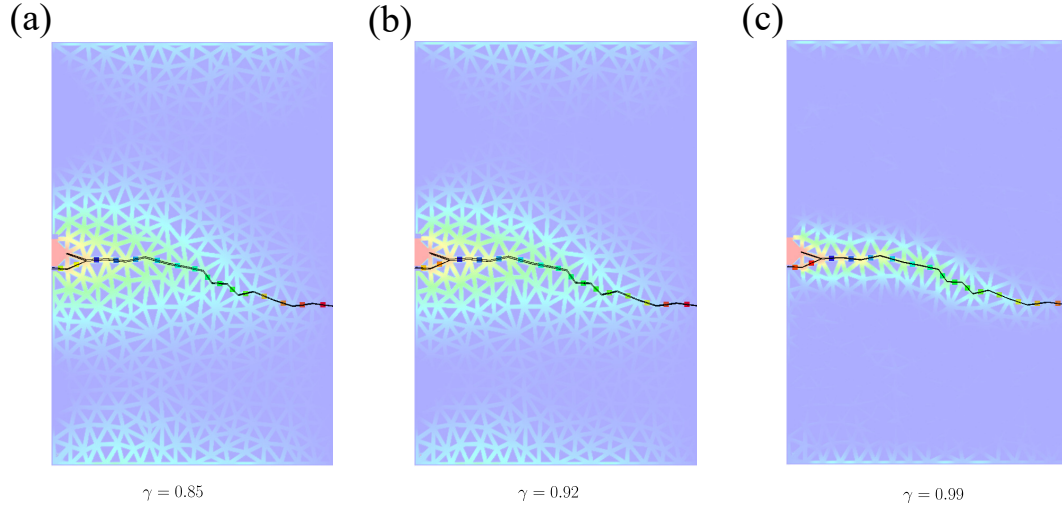
446

449

450

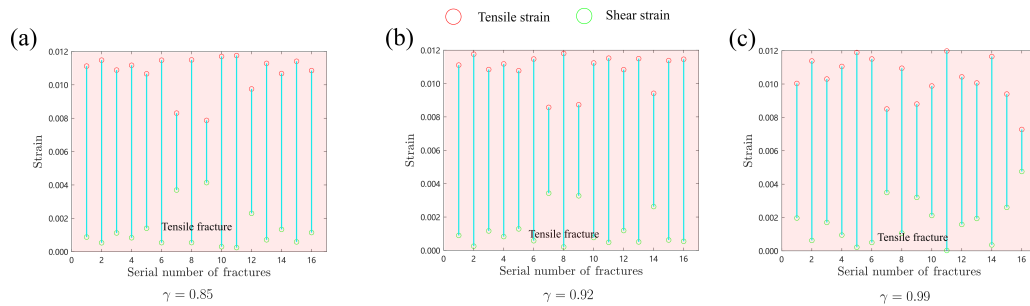
higher the fracture initiation pressure is, which is consistent with the observations in the

451 lab experiments (Fazio et al., 2021). The fracture geometries are similar for all cases,
 452 which are horizontal. Three examples with $\gamma = 0.85, 0.92$ and 0.99 are shown in Fig. 20.
 453 The corresponding strain components of each fracture are shown in Fig. 21. All generated
 fractures are tensile fractures with insignificant shear strain.



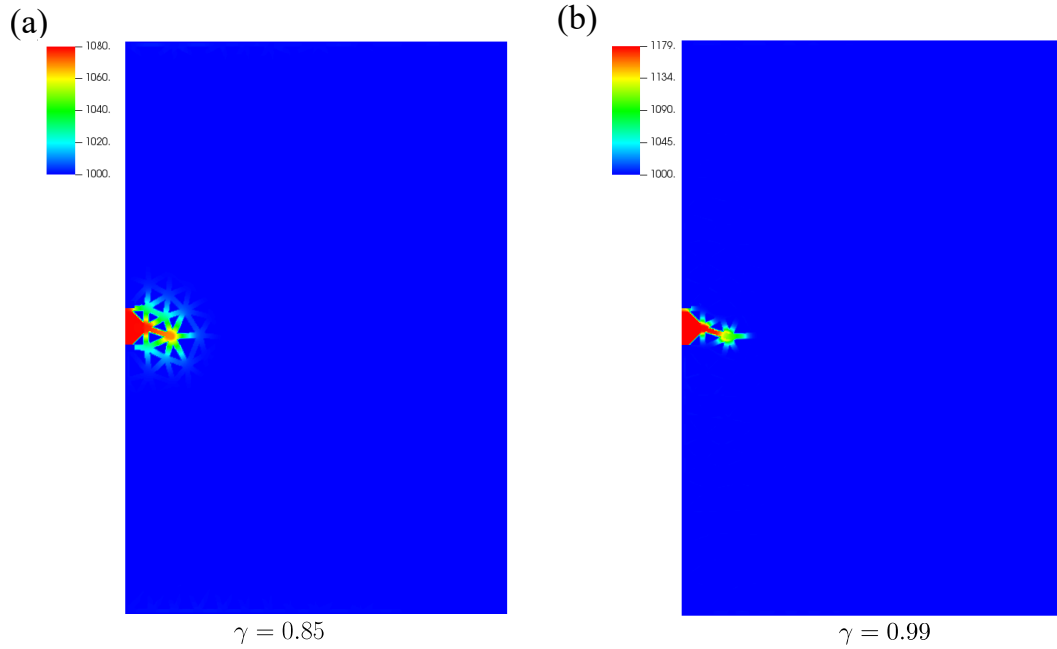
447 **Figure 20.** Fracture geometries of cases with different formation permeability at 0.04s

454



455 **Figure 21.** Tensile and shear strain of each fracture segment in Fig. 20

458 The matrix permeability controls the leakage of fluid as shown in Fig. 20. The pressure
 459 propagates to a larger region in a highly permeable case (Fig. 20a) and the influential region
 460 is quite narrow for the weakly permeability cases (Fig. 20c). To better demonstrate this
 461 phenomenon, the pressure distributions at the fracture initiation of the case with $\gamma = 0.85$
 462 and $\gamma = 0.99$ are shown in Fig. 22. For the case with $\gamma = 0.99$, the pore pressure is quite
 463 high in the cave and the preset fracture but hardly propagates to the neighboring region.
 464 For the case with $\gamma = 0.85$, the pressure propagates to a much larger region.



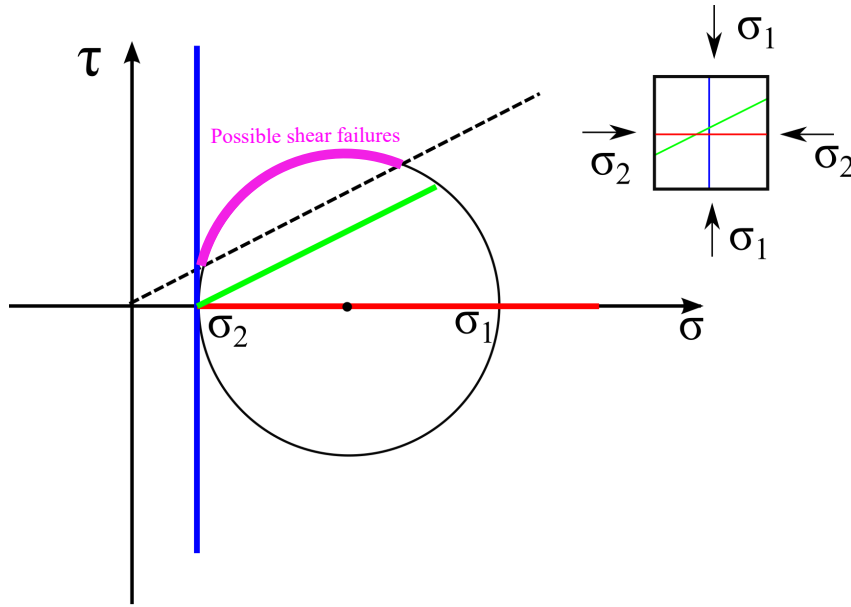
456 **Figure 22.** Pore pressure distribution at the fracture initiation stage for cases with a high (a)
 457 and low (b) formation permeability, respectability

465 4 Discussions

466 In this work, we conducted a systematical analysis of the impacts of different factors
 467 (formation parameters, treatment parameters, and rock properties) on the fracture initiation
 468 and propagation process. The impact of each factor is evaluated with the other factors fixed.
 469 It is beneficial to first have an independent factor analysis and provide a comprehensive and
 470 detailed understanding of each factor. Subsequently, analysis of coupled effects or impacts
 471 of interactions between different factors can be extended, which is technically available with
 472 the foundation constructed in this work. In addition, with optimization of the algorithm
 473 efficiency and development of new modulus, more factors, such as temperature, grain size,
 474 different injection schemes, can be considered in the future for more complex scenarios.

475 Most primary hydraulic fractures (horizontal ones in most cases) are tensile fractures.
 476 However, when the primary fracture reaches the right boundary, vertical tensile fractures
 477 are possible if the pore pressure is high enough. In the transition zone, shear fractures
 478 are more dominant than tensile fractures, like Fig. 3(d-f), Fig. 7(b), and Fig. 15(a-c). The
 479 generated shear fractures are usually inclined and a Mohr's circle analysis may explain this
 480 phenomenon. In Fig. 23, a Mohr's circle and stress states of three planes (blue, green, and

481 red) are determined by the intersection point between the plane and the Mohr's circle. For
 482 the demonstration purpose, the friction coefficient is 0.4 and the cohesion strength is set to
 483 zero. The specific Mohr's circle in the simulation domain is caused by the enhanced pore
 484 pressure from leak-off and principle stresses generated by the compression from the primary
 485 hydraulic fracture. The purple arc in Morh's circle refers to all possible plane directions
 486 that can trigger a shear failure. The inclined bonds are more likely to form shear failures
 487 because their orientations fall into the shear failure range.



488 **Figure 23.** A sketch map of a Mohr's circle for different fracture planes (red, blue, and green)

489 The DEM-LBM coupled method is powerful to investigate the detailed fracture initia-
 490 tion and propagation process. However, there are still several limitations and two important
 491 ones are listed below:

- 492 • The roughness of the fracture surface is difficult to be reproduced with DEM since
 493 there are large differences in scales between the particle size and asperity size. There-
 494 fore the shear dilation process is hard to mimic, which is also an important mechanism
 495 to form complex fracture networks in a hydraulic fracturing process (Rahman et al.,
 496 2002).
- 497 • The breakage of particles is not applicable in this DEM scheme. Therefore, only
 498 breakage between particles is possible. However, several experiments observed that

499 hydraulic fractures can cut the minerals and propagate across particles, especially in
500 hydraulic fracturing with critical CO₂ (Y. Chen et al., 2015),

501 Therefore, improvements in the numerical scheme or the development of new schemes are
502 still necessary to simulate the hydraulic fracturing process in reality.

503 **5 Conclusions**

504 In this work, a comprehensive investigation of the influential factors on the initiation
505 and propagation in a hydraulic fracturing process is conducted with the DEM-LBM method.
506 The factors include formation parameters (in-situ stress states), treatment parameters
507 (injection rates and fluid viscosity), and rock properties (heterogeneity of rock strengths
508 and formation permeability). Several important findings and conclusions are drawn below:

- 509 • All factors have a significant impact on the fracture initiation pressure. A higher
510 injection rate, higher viscosity, and larger in-situ stress will increase the initiation
511 pressure, while a higher formation permeability and higher heterogeneity degree of
512 bond strengths will decrease the initiation pressure.
- 513 • Injection rate and heterogeneity degree have much significant impact on the com-
514 plexity of generated fractures. Fluid viscosity, in-situ stress states, and formation
515 permeability do not change the geometrical complexity.
- 516 • Hydraulic fractures are usually tensile fractures, however, they usually do not have
517 pure tensile displacement. Shear fractures are possible and the shear displacement
518 can be significant under certain conditions, such as a high injection rate, and high
519 heterogeneity degrees.

520 **Acknowledgments**

521 This project was supported by the National Key Research and Development Program of
522 China (No. 2019YFA0708704). The authors would like to thank all editors and anonymous
523 reviewers for their comments and suggestions.

524 Data Availability Statement

525 The numerical simulation in this work is based on the open-source multi-physics simu-
 526 lation library MECHSYS developed by Dr. S.A. Galindo Torres. The library is available at
 527 <https://mechsys.nongnu.org/>.

528 Appendix A Benchmark case for LBM simulation

529 The Poiseuille flow in a slit driven by gravity is chosen as the benchmark case to
 530 validate the LBM algorithm. The slit has lengths and widths of 100 and 48 lattice units
 531 (lu). A bounce-back boundary condition is implemented on the top and bottom walls. A
 532 periodic boundary condition is adopted to avoid the entry or exit effect for the left and right
 533 boundaries.

534 The Reynolds number is 20 to ensure a laminar flow state. The maximum velocity
 535 (u_{max}) is chosen as $0.1 lu ts^{-1}$. The relaxation time (τ) is 1.0 for the simple bounce-
 536 back boundaries, which yield a kinematic viscosity (ν) of $1/6 lu^2 ts^{-1}$. Fluid density (ρ)
 537 is chosen as 1.0. The analytical solution for the gravity-driven Poiseuille flow yields a
 538 parabolic velocity profile:

$$u(x) = \frac{\rho g}{2\mu}(a^2 - x^2), \quad (A1)$$

539 where $u(x)$ is the velocity in the Y direction, a is the half width of the slit, g is the gravi-
 540 tational acceleration. The maximum velocity is :

$$u_{max} = \frac{\rho g a^2}{2\mu} \quad (A2)$$

541 Through rearranging Eq. A2, the corresponding gravitational acceleration (g) to drive the
 542 flow is calculated:

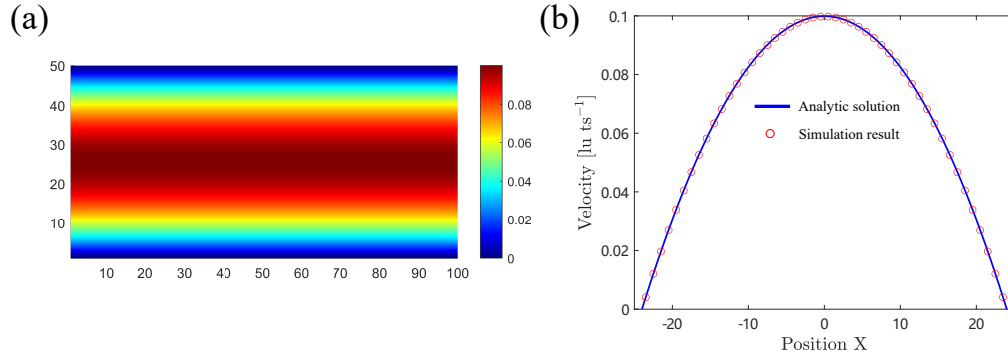
$$g = \frac{2\nu u_{max}}{a^2} \quad (A3)$$

543 Therefore, g is $5.7804 \times 10^{-5} lu ts^{-2}$.

546 The velocity distribution in the slit is shown in Fig. A1(a) and Fig. A1(b) shows the
 547 comparison between the analytical solution and the simulation result.

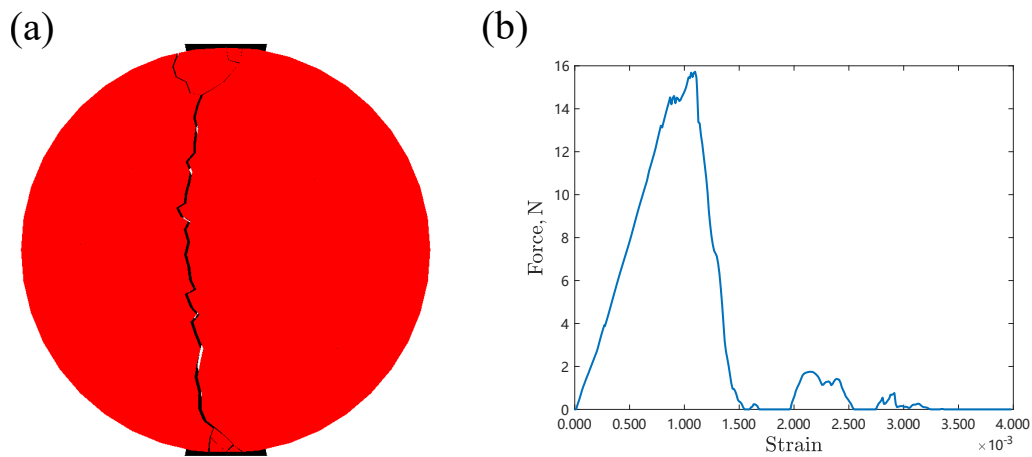
548 Appendix B Benchmark case for the DEM simulation

549 A Brazilian test is used to validate the correctness of the DEM simulation. A round
 550 disc with a diameter of 0.2 m and a thickness of 0.1 m is generated for the simulation. The



544 **Figure A1.** (a) The velocity distribution in a slit (b) Comparison between the analytical solution
 545 and LBM result

551 total number of particles is 1,924. The specific rock properties are not used in the simu-
 552 lation considering the computational cost. The normal and tangential contact stiffness are
 553 $1.0 \times 10^5 \text{N/m}$. The normal and tangential elastic modulus are $1.0 \times 10^5 \text{Pa}$. The threshold
 554 value on the total strain is 0.02. The time step is chosen as $4.5 \times 10^{-5} \text{s}$. The breaking results
 555 after the compression are shown in Fig. B1. A vertical fracture and V-shaped damage zones
 556 are observed, and similar results are found in lab experiments (Gong et al., 2019).



557 **Figure B1.** (a) Fractures formed after compression in a Brazilian test (b) The force-strain
 558 relation of the Brazilian test

References

- 559
- 560 Buckingham, E. (1915). The principle of similitude. *Nature*, *96*(2406), 396–397.
- 561 Chen, H., Meng, X., Niu, F., Tang, Y., Yin, C., & Wu, F. (2018). Microseismic monitoring
562 of stimulating shale gas reservoir in sw china: 2. spatial clustering controlled by the
563 preexisting faults and fractures. *Journal of Geophysical Research: Solid Earth*, *123*(2),
564 1659–1672.
- 565 Chen, S., & Doolen, G. D. (1998). Lattice boltzmann method for fluid flows. *Annual review*
566 *of fluid mechanics*, *30*(1), 329–364.
- 567 Chen, Y., Nagaya, Y., & Ishida, T. (2015). Observations of fractures induced by hydraulic
568 fracturing in anisotropic granite. *Rock Mechanics and Rock Engineering*, *48*(4), 1455–
569 1461.
- 570 Chen, Z., Elsworth, D., & Wang, M. (2020). Does low-viscosity fracturing fluid always
571 create complex fractures? *Journal of Geophysical Research: Solid Earth*, *125*(9),
572 e2020JB020332.
- 573 Chen, Z., Jin, X., & Wang, M. (2018). A new thermo-mechanical coupled dem model with
574 non-spherical grains for thermally induced damage of rocks. *Journal of the Mechanics*
575 *and Physics of Solids*, *116*, 54–69.
- 576 Chen, Z., & Wang, M. (2017). Pore-scale modeling of hydromechanical coupled mechanics
577 in hydrofracturing process. *Journal of Geophysical Research: Solid Earth*, *122*(5),
578 3410–3429.
- 579 Chen, Z., & Wang, M. (2020). An improved immersed moving boundary for hydrodynamic
580 force calculation in lattice boltzmann method. *International Journal for Numerical*
581 *Methods in Engineering*, *121*(20), 4493–4508.
- 582 Cheng, S., Zhang, M., Zhang, X., Wu, B., Chen, Z., Lei, Z., & Tan, P. (2022). Numerical
583 study of hydraulic fracturing near a wellbore using dual boundary element method.
584 *International Journal of Solids and Structures*, *239*, 111479.
- 585 Cundall, P. A., & Strack, O. D. (1979). A discrete numerical model for granular assemblies.
586 *geotechnique*, *29*(1), 47–65.
- 587 Dahi-Taleghani, A., & Olson, J. E. (2011). Numerical modeling of multistranded-hydraulic-
588 fracture propagation: accounting for the interaction between induced and natural
589 fractures. *SPE journal*, *16*(03), 575–581.
- 590 De Pater, C., & Beugelsdijk, L. (2005). Experiments and numerical simulation of hydraulic
591 fracturing in naturally fractured rock. In *Alaska rocks 2005, the 40th us symposium*

- 592 *on rock mechanics (usrms)*.
- 593 Duan, K., Kwok, C. Y., Wu, W., & Jing, L. (2018). Dem modeling of hydraulic fractur-
594 ing in permeable rock: influence of viscosity, injection rate and in situ states. *Acta*
595 *Geotechnica*, *13*(5), 1187–1202.
- 596 Fazio, M., Ibemesi, P., Benson, P., Bedoya-González, D., & Sauter, M. (2021). The role
597 of rock matrix permeability in controlling hydraulic fracturing in sandstones. *Rock*
598 *Mechanics and Rock Engineering*, *54*(10), 5269–5294.
- 599 Galindo-Torres, S. (2013). A coupled discrete element lattice boltzmann method for the sim-
600 ulation of fluid–solid interaction with particles of general shapes. *Computer Methods*
601 *in Applied Mechanics and Engineering*, *265*, 107–119.
- 602 Galindo-Torres, S. A., Alonso-Marroquín, F., Wang, Y., Pedroso, D., & Castano, J. M.
603 (2009). Molecular dynamics simulation of complex particles in three dimensions and
604 the study of friction due to nonconvexity. *Physical Review E*, *79*(6), 060301.
- 605 Galindo-Torres, S. A., Pedroso, D., Williams, D., & Li, L. (2012). Breaking processes in
606 three-dimensional bonded granular materials with general shapes. *Computer Physics*
607 *Communications*, *183*(2), 266–277.
- 608 Gandossi, L., & Von Estorff, U. (2013). An overview of hydraulic fracturing and other
609 formation stimulation technologies for shale gas production. *Eur. Commisison Jt.*
610 *Res. Cent. Tech. Reports*, *26347*.
- 611 Gong, F., Zhang, L., & Wang, S. (2019). Loading rate effect of rock material with the direct
612 tensile and three brazilian disc tests. *Advances in Civil Engineering*, *2019*.
- 613 Goodfellow, S., Nasser, M., Maxwell, S., & Young, R. (2015). Hydraulic fracture energy
614 budget: Insights from the laboratory. *Geophysical Research Letters*, *42*(9), 3179–3187.
- 615 Heider, Y. (2021). A review on phase-field modeling of hydraulic fracturing. *Engineering*
616 *Fracture Mechanics*, *253*, 107881.
- 617 Huang, B., & Liu, J. (2017). Experimental investigation of the effect of bedding planes on
618 hydraulic fracturing under true triaxial stress. *Rock Mechanics and Rock Engineering*,
619 *50*(10), 2627–2643.
- 620 Kumari, W., Ranjith, P., Perera, M., Li, X., Li, L., Chen, B., ... De Silva, V. (2018).
621 Hydraulic fracturing under high temperature and pressure conditions with micro ct
622 applications: geothermal energy from hot dry rocks. *Fuel*, *230*, 138–154.
- 623 Lecampion, B. (2009). An extended finite element method for hydraulic fracture problems.
624 *Communications in Numerical Methods in Engineering*, *25*(2), 121–133.

- 625 Liu, P., Ju, Y., Gao, F., Ranjith, P. G., & Zhang, Q. (2018). Ct identification and frac-
626 tal characterization of 3-d propagation and distribution of hydrofracturing cracks in
627 low-permeability heterogeneous rocks. *Journal of Geophysical Research: Solid Earth*,
628 *123*(3), 2156–2173.
- 629 Liu, P., Ju, Y., Ranjith, P. G., Zheng, Z., Wang, L., & Wanniarachchi, A. (2016). Visual
630 representation and characterization of three-dimensional hydrofracturing cracks within
631 heterogeneous rock through 3d printing and transparent models. *International Journal*
632 *of Coal Science & Technology*, *3*(3), 284–294.
- 633 Mohammadnejad, T., & Khoei, A. (2013). An extended finite element method for hydraulic
634 fracture propagation in deformable porous media with the cohesive crack model. *Finite*
635 *Elements in Analysis and Design*, *73*, 77–95.
- 636 Morgan, S., Li, B., & Einstein, H. (2017). Effect of injection rate on hydraulic fracturing
637 of opalinus clay shale. In *51st us rock mechanics/geomechanics symposium*.
- 638 Nagaso, M., Mikada, H., & Takekawa, J. (2015). The role of fluid viscosity in hydraulic
639 fracturing in naturally fractured rock. In *Seg technical program expanded abstracts*
640 *2015* (pp. 3214–3218). Society of Exploration Geophysicists.
- 641 Noble, D., & Torczynski, J. (1998). A lattice-boltzmann method for partially saturated
642 computational cells. *International Journal of Modern Physics C*, *9*(08), 1189–1201.
- 643 Olson, J. E., & Taleghani, A. D. (2009). Modeling simultaneous growth of multiple hydraulic
644 fractures and their interaction with natural fractures. In *Spe hydraulic fracturing*
645 *technology conference*.
- 646 O’Sullivan, C., & Bray, J. D. (2004). Selecting a suitable time step for discrete element
647 simulations that use the central difference time integration scheme. *Engineering Com-*
648 *putations*.
- 649 Pan, X.-H., Xiong, Q.-Q., & Wu, Z.-J. (2018). New method for obtaining the homogeneity
650 index m of weibull distribution using peak and crack-damage strains. *International*
651 *Journal of Geomechanics*, *18*(6), 04018034.
- 652 Papachristos, E., Scholtès, L., Donzé, F., & Chareyre, B. (2017). Intensity and volumetric
653 characterizations of hydraulically driven fractures by hydro-mechanical simulations.
654 *International Journal of Rock Mechanics and Mining Sciences*, *93*, 163–178.
- 655 Peirce, A., & Detournay, E. (2009). An eulerian moving front algorithm with weak-form tip
656 asymptotics for modeling hydraulically driven fractures. *Communications in numerical*
657 *methods in engineering*, *25*(2), 185–200.

- 658 Pruess, K. (2006). Enhanced geothermal systems (egs) using co2 as working fluid—a novel
659 approach for generating renewable energy with simultaneous sequestration of carbon.
660 *Geothermics*, 35(4), 351–367.
- 661 Rahman, M., Hossain, M., & Rahman, S. (2002). A shear-dilation-based model for evalua-
662 tion of hydraulically stimulated naturally fractured reservoirs. *International Journal*
663 *for Numerical and Analytical Methods in Geomechanics*, 26(5), 469–497.
- 664 Shimizu, H., Murata, S., & Ishida, T. (2011). The distinct element analysis for hydraulic
665 fracturing in hard rock considering fluid viscosity and particle size distribution. *Inter-*
666 *national journal of rock mechanics and mining sciences*, 48(5), 712–727.
- 667 Stanchits, S., Surdi, A., Gathogo, P., Edelman, E., & Suarez-Rivera, R. (2014). Onset of hy-
668 draulic fracture initiation monitored by acoustic emission and volumetric deformation
669 measurements. *Rock Mechanics and Rock Engineering*, 47(5), 1521–1532.
- 670 Van Mier, J. G., van Vliet, M. R., & Wang, T. K. (2002). Fracture mechanisms in particle
671 composites: statistical aspects in lattice type analysis. *Mechanics of Materials*, 34(11),
672 705–724.
- 673 Wang, Y., Li, X., & Tang, C. (2016). Effect of injection rate on hydraulic fracturing
674 in naturally fractured shale formations: a numerical study. *Environmental Earth*
675 *Sciences*, 75(11), 1–16.
- 676 Wangen, M. (2011). Finite element modeling of hydraulic fracturing on a reservoir scale in
677 2d. *Journal of Petroleum Science and Engineering*, 77(3-4), 274–285.
- 678 Warpinski, N., Wolhart, S., & Wright, C. (2004). Analysis and prediction of microseismicity
679 induced by hydraulic fracturing. *Spe Journal*, 9(01), 24–33.
- 680 Warpinski, N. R., Wolhart, S., Wright, C., et al. (2001). Analysis and prediction of mi-
681 croseismicity induced by hydraulic fracturing. In *Spe annual technical conference and*
682 *exhibition*.
- 683 Wilson, Z. A., & Landis, C. M. (2016). Phase-field modeling of hydraulic fracture. *Journal*
684 *of the Mechanics and Physics of Solids*, 96, 264–290.
- 685 Yousefi, A., & Ng, T.-T. (2017). Dimensionless input parameters in discrete element model-
686 ing and assessment of scaling techniques. *Computers and Geotechnics*, 88, 164–173.
- 687 Yushi, Z., Shicheng, Z., Tong, Z., Xiang, Z., & Tiankui, G. (2016). Experimental inves-
688 tigation into hydraulic fracture network propagation in gas shales using ct scanning
689 technology. *Rock Mechanics and Rock Engineering*, 49(1), 33–45.
- 690 Zeng, Z., & Roegiers, J.-C. (2002). Experimental observation of injection rate influence on

- 691 the hydraulic fracturing behavior of a tight gas sandstone. In *Spe/isrm rock mechanics*
692 *conference*.
- 693 Zhao, X., Huang, B., & Xu, J. (2019). Experimental investigation on the characteristics of
694 fractures initiation and propagation for gas fracturing by using air as fracturing fluid
695 under true triaxial stresses. *Fuel*, *236*, 1496–1504.
- 696 Zhao, Y., Zhang, Y., Wang, C., & Liu, Q. (2022). Hydraulic fracturing characteristics and
697 evaluation of fracturing effectiveness under different anisotropic angles and injection
698 rates: an experimental investigation in absence of confining pressure. *Journal of*
699 *Natural Gas Science and Engineering*, *97*, 104343.
- 700 Zhu, W., He, X., Khirevich, S., & Patzek, T. W. (2022). Fracture sealing and its impact on
701 the percolation of subsurface fracture networks. *J. Pet. Sci. Eng.*, *218*, 111023.
- 702 Zhuang, L., Kim, K. Y., Jung, S. G., Diaz, M., & Min, K.-B. (2019). Effect of water
703 infiltration, injection rate and anisotropy on hydraulic fracturing behavior of granite.
704 *Rock Mechanics and Rock Engineering*, *52*(2), 575–589.
- 705 Zhuang, L., & Zang, A. (2021). Laboratory hydraulic fracturing experiments on crystalline
706 rock for geothermal purposes. *Earth-Science Reviews*, *216*, 103580.

Numerical Investigation of Influential Factors in Hydraulic Fracturing Processes Using Coupled Discrete Element-Lattice Boltzmann Method

Weiwei Zhu¹, Zhiqiang Chen², Zhiguo Tian¹, Moran Wang¹

¹Department of Engineering Mechanics, Tsinghua University, Beijing, China

²Petroleum Exploration and Production Research Institute, SINOPEC, Beijing, China

Key Points:

- Different influential factors have significant impacts on the initiation pressure.
- High injection rates and heterogeneity degrees increase the geometrical complexity of fractures.
- Hydraulic fractures are dominated by tensile fractures, but shear fractures are also possible.

Abstract

Hydraulic fracturing is widely used to stimulate unconventional reservoirs, but a systematic and comprehensive investigation into the hydraulic fracturing process is rare. In this work, a discrete element-lattice Boltzmann method is implemented to simulate the hydro-mechanical behavior in a hydraulic fracturing process. Different influential factors, including injection rates, fluid viscosity, in-situ stress states, heterogeneity of rock strengths, and formation permeability, are considered and their impacts on the initiation and propagation of hydraulic fractures are evaluated. All factors have a significant impact on the fracture initiation pressure. A higher injection rate, higher viscosity, and larger in-situ stress increase the initiation pressure, while a higher formation permeability and higher heterogeneity decrease the initiation pressure. Injection rates and heterogeneity degrees have significant impacts on the complexity of generated fractures. Fluid viscosity, in-situ stress states, and formation permeability do not change the geometrical complexity significantly. Hydraulic fractures are usually tensile fractures, but many tensile fractures also have shear displacement. Shear

Corresponding author: Moran Wang, mrwang@tsinghua.edu.cn

fractures are possible and the shear displacement can be significant under certain conditions, such as a high injection rate, and a high heterogeneity degree.

Plain Language Summary

Hydraulic fracturing technique is essential for the development of unconventional reserves, such as shale gas, shale oil, and geothermal reservoirs. To optimize hydraulic fracturing operations and enhance recovery efficiency, it is necessary to understand the process's mechanism and figure out the influential factors. Direct observations of the hydraulic fracturing process in the subsurface are impossible. In this work, we adopt a numerical scheme (DEM-LBM) to investigate the process in detail and consider as many factors as possible, including injection rates, fluid viscosity, in-situ stress states, heterogeneity of rock strengths, and formation permeability. The impacts of those influential factors on the initiation and propagation of hydraulic fractures are evaluated. We find that all factors have a significant impact on fracture initiation pressure. However, the complexity of generated fractures is mainly affected by injection rates and heterogeneity degrees of rock strengths. Generated hydraulic fractures are usually tensile fractures, but shear fractures are possible and the shear displacement can be significant under certain conditions, such as a high injection rate, and a high heterogeneity degree. Continued research is required to further include the interactions between factors and it is completely possible with the foundation constructed in this work.

1 Introduction

Hydraulic fracturing refers to the process of injecting highly-pressurized liquid into a well to break up bedrock formations, which is vastly implemented in stimulating unconventional reservoirs, e.g. shale oil, shale gas, and enhanced geothermal systems (Pruess, 2006; Gandossi & Von Estorff, 2013).

The hydraulic fracture process is quite complex and cannot be observed directly in the deep subsurface. Microseismicity techniques are effective to locate fracture events and distinguish failure modes but cannot provide detailed information on fracture initiation and propagation (N. Warpinski et al., 2004; H. Chen et al., 2018). Therefore, many lab experiments and numerical simulations are conducted to investigate the hydraulic fracturing process. Experiments under triaxial and true triaxial stress conditions are widely adopted to mimic the actual geostress states (Huang & Liu, 2017; X. Zhao et al., 2019). The

58 acoustic emission method is used to monitor the hydraulic fracturing process (Stanchits
59 et al., 2014; Goodfellow et al., 2015), but similar to the microseismicity method in the
60 field, detailed morphology information of fractures is not available. To observe the fracture
61 morphologies inside rock samples, Liu et al. (2018) experimentally investigated the hydraulic
62 fracturing process in heterogeneous samples under different stress anisotropy levels and the
63 morphological patterns of hydraulic fractures are identified with CT scanning. Similar
64 methods are adopted by Yushi et al. (2016), Kumari et al. (2018), and many others. CT
65 scanning method is limited to the resolution and long operation time, which is difficult to
66 capture the real-time variations of fracture initiation and propagation process. In addition,
67 hydraulic fracturing experiments are destructive experiments, which means the samples are
68 not reusable after fracking. 3D-printed samples can reproduce the same rock samples and
69 optical visualization is available (Liu et al., 2016), but the printing materials are usually
70 far different from actual rocks in terms of physical and mechanical properties. Also, having
71 a comprehensive investigation of the influential factors requires a large number of rock
72 samples, which is both time-consuming and financially expensive.

73 Numerical simulation of the hydraulic fracturing process is a useful way to conduct
74 sensitivity analysis of influential factors. The hydraulic fracturing process is a strongly cou-
75 pled hydro-mechanical process. For the mechanical part, several continuum and mesoscale
76 numerical methods are used to simulate fracture initiation and propagation. The continuum
77 methods mainly include the boundary element method (Olson & Taleghani, 2009; Cheng et
78 al., 2022), extended finite element method (XFEM) (Dahi-Taleghani & Olson, 2011; Mo-
79 hammadnejad & Khoei, 2013), and phase field methods (Wilson & Landis, 2016; Heider,
80 2021). However, the continuum method usually involves high requirements for mesh quality
81 and complicated treatments for complex boundary conditions. Therefore, the mesoscale
82 numerical method is also widely used to simulate mechanical deformation, which mainly
83 refers to the discrete element method (DEM). DEM directly describes the mechanical dis-
84 placements and interactions of discontinues particles (Cundall & Strack, 1979). For the
85 fluid dynamics part, the assumption of lubrication flow is usually used since a fracture
86 has a width significantly smaller than its length. The finite volume method (FVM) and
87 finite element method (FEM) can be used to discretize and solve the flow equations and
88 couple with mechanical part (Peirce & Detournay, 2009; Lecampion, 2009; Wangen, 2011;
89 Papachristos et al., 2017). However, the lattice Boltzmann method (LBM) has several ad-
90 vantages compared with FVM and FEM, such as simple calculation procedures, convenient

91 implementation of parallel computation, and simple treatment of complex geometries. In
92 addition, through the Chapman-Enskog theory, the Navier-Stokes equations can be derived
93 from the Boltzmann equation (S. Chen & Doolen, 1998). Therefore, the LBM method can
94 solve the Navier-Stokes equations and overcome the possible inaccuracy caused by the lu-
95 brication flow assumption. Coupled DEM-LBM method is a good option for simulating the
96 hydro-mechanical coupling process (S. A. Galindo-Torres et al., 2012; S. Galindo-Torres,
97 2013; Z. Chen & Wang, 2017; Z. Chen et al., 2020).

98 Many factors can influence the geometry of hydraulic fractures, like formation parame-
99 ters (e.g. in-situ stress), treatment parameters (e.g. injection rate and fluid viscosity), and
100 rock properties (e.g. rock strength heterogeneity and formation permeability). Zeng and
101 Roegiers (2002); De Pater and Beugelsdijk (2005); Liu et al. (2018); Zhuang et al. (2019);
102 Fazio et al. (2021) and Y. Zhao et al. (2022) investigated the impact of injection rate, fluid
103 viscosity, stress states, and matrix permeability on the hydraulic fracturing process with
104 lab experiments. The results provide helpful insights, but lab experiments cannot use an
105 identical rock sample in each test. A strict factor control leads to a large number of indi-
106 vidual experiments and lab experiments usually cannot exclude the impact of intrinsic rock
107 characteristics, such as the heterogeneity of natural rocks. In contrast, numerical simula-
108 tions can have better factor controls and investigate the impact of each factor. Nagaso et
109 al. (2015); Wang et al. (2016); Z. Chen et al. (2020) and Duan et al. (2018) investigated
110 the impact of fluid viscosity, injection rate, and in-situ states on the fracture propagation
111 process through different numerical methods. However, a comprehensive investigation of
112 the hydraulic fracturing process considering all the influential factors mentioned above is
113 rare (Zhuang & Zang, 2021). In this work, we aim to have a comprehensive investigation
114 considering the impacts of injection rate, fluid viscosity, heterogeneity of rock strength, for-
115 mation permeability, and in-situ stress state on the initiation and propagation of hydraulic
116 fractures, which is helpful to deepen the understanding of hydraulic fracturing processes.

117 In this work, a DEM-LBM method is adopted to simulate the hydraulic fracturing
118 process, and Section. 2 introduces detailed information about the coupled method. Impacts
119 of different factors on fracture initiation and propagation are demonstrated in Section. 3. In
120 Section. 4, we discuss the limitation of the method and possible improvements. Important
121 conclusions are summarized in Section. 5.

2 Methods and materials

2.1 A DEM-LBM scheme for the simulation of hydraulic fracturing process

A DEM-LBM method is adopted in this work to simulate the coupled hydro-mechanical process. The numerical framework is based on the multi-physics simulation software MECHSYS developed by S. Galindo-Torres (2013) and extension of the software developed by Z. Chen and Wang (2017) and Z. Chen et al. (2018, 2020). Only a brief introduction of the method is covered in this section and more detailed information is available in the references above.

DEM treats materials as an assembly of discrete particles. In this work, the interactions between particles are approximated with linear contact and bonding models. In the linear contact model, the contact can happen between different geometrical patterns of two particles, including edge-edge and vertex-face for polyhedrons (S. A. Galindo-Torres et al., 2012). The normal elastic force \vec{F}_n^c between different geometrical pairs (P_i and P_j) is given by:

$$\vec{F}_n^c(P_i, P_j) = K_n \vec{\delta}(P_i, P_j), \quad (1)$$

Where K_n is the normal contact stiffness, $\vec{\delta}(P_i, P_j)$ is the normal displacement (overlapping) vector between a geometric pattern pair. The net elastic force is the summation of forces for all pairs of geometrical patterns.

Similarly, the tangential contact force \vec{F}_t^c is given by:

$$\vec{F}_t^c = K_t \vec{\zeta}(P_i, P_j), \quad (2)$$

where K_t is the tangential contact stiffness and $\vec{\zeta}(P_i, P_j)$ is the tangential displacement vector between a geometric pattern pair.

In the bonding model, two neighboring spheropolyhedra sharing a common face are connected with an elastic force. The cohesive force in the normal direction \vec{F}_n^b is given by:

$$\vec{F}_n^b = B_n A \vec{\epsilon}_n, \quad (3)$$

where B_n is the normal elastic modulus of the material, A is the shared face area between particles, and $\vec{\epsilon}_n$ is the normal strain in the direction normal to the common face and positive for tensile deformation. The normal cohesive force is calculated for tensile deformation only and Eq. 1 accounts for the normal elastic force in a compressive deformation.

148 The cohesive force in the tangential direction \vec{F}_t^b is given by:

$$\vec{F}_t^b = B_t A \vec{\epsilon}_t, \quad (4)$$

149 where B_t is the tangential elastic modulus of the material, and $\vec{\epsilon}_t$ is the shear strain in the
150 direction tangential to the common face.

151 A threshold value on the total strain, denoted as ϵ_{th} , is provided as the criterion of
152 fracture initiation:

$$|\vec{\epsilon}_n| + |\vec{\epsilon}_t| \geq \epsilon_{th}, \quad (5)$$

153 where $\vec{\epsilon}_n$ and $\vec{\epsilon}_t$ are the normal and tangential strain caused by the displacement of adjacent
154 faces.

155 A broken bond is classified as a shear failure if its shear strain is larger than the normal
156 strain. Similarly, a tensile failure refers to a case where the tensile strain is larger than the
157 shear strain. A similar classification is adopted in Shimizu et al. (2011) and Z. Chen and
158 Wang (2017).

159 The lattice Boltzmann method (LBM) is a useful computational fluid dynamics method
160 for fluid simulation, where the fluid is regarded as fictive particles, and the density distri-
161 bution functions of particles are simulated through streaming and collision processes. In
162 this work, a D3Q15 model is chosen to simulate the fluid flow considering the accuracy and
163 computation efficiency. The corresponding evolution equation is:

$$f_i(\vec{x} + \vec{e}_i \delta t, t + \delta t) = f_i(\vec{x}, t) - \frac{\delta t}{\tau} (f_i(\vec{x}, t) - f_i^{eq}(\vec{x}, t)), \quad i = 0, 1, 2 \dots 14, \quad (6)$$

164 where f_i and f_i^{eq} are the density distribution function and the corresponding equilibrium
165 distribution in the i th discrete velocity direction, \vec{e}_i , δt is the time step adopted in the
166 simulation, and τ is the relaxation time. Through the Chapman-Enskog analysis, the fluid
167 kinematic shear viscosity ν is related to τ by:

$$\nu = \frac{1}{3} c^2 \left(\tau - \frac{\delta t}{2} \right), \quad (7)$$

168 where c is the lattice speed in LBM. Note that all parameters in lattice Boltzmann equations
169 are dimensionless with "lattice units". To map the lattice units to physical units, proper
170 conversion factors are required. A set of basic conversion factors, composed of time, length,
171 and mass, is sufficient to derive the dimension of any physical parameters in this work. The
172 corresponding basic conversion factors are C_l , C_t , and C_ρ , since the length, time and density

173 are natural quantities in LB simulations.

$$C_l = \frac{\delta x^*}{\delta x} \quad (8)$$

$$C_t = \frac{\delta t^*}{\delta t} \quad (9)$$

$$C_\rho = \frac{\rho^*}{\rho} \quad (10)$$

176 Note that the parameters with * have physical units. δx and δt are the grid size and time
 177 step used in the simulation. Usually, δx and δt are 1 in LBM implementation and we use
 178 the physical density as the lattice density. Therefore, the corresponding conversion factors
 179 are $C_l = \delta x^*$, $C_t = \delta t^*$, and $C_\rho = 1$. The conversion factor for ν can be obtained through a
 180 simple dimension analysis:

$$C_\nu = \frac{C_l^2}{C_t} \quad (11)$$

181 Therefore, the physical kinematic viscosity of the simulated fluid is

$$\nu^* = \frac{1}{3} \left(\tau - \frac{1}{2} \right) \frac{\delta^2 x^*}{\delta t^*} \quad (12)$$

182 The fluid density and velocity can be obtained from the density distribution function:

$$\rho = \sum_i f_i \quad (13)$$

$$\vec{u} = \frac{\sum_i f_i \vec{e}_i}{\rho} \quad (14)$$

184 The pressure can also be obtained from the Chapman-Enskog analysis:

$$p = \frac{1}{3} \rho c^2 \quad (15)$$

185 In the fluid simulation, we care more about the pressure difference concerning the initial
 186 pressure instead of the specific pressure. Therefore, with a proper conversion factor, the
 187 physical pressure difference can be calculated by:

$$\Delta p^* = \frac{1}{3} \Delta \rho \frac{\delta^2 x^*}{\delta^2 t^*} \quad (16)$$

188 An immersed boundary method (IBM) is applied to incorporate the fluid-solid inter-
 189 actions (Noble & Torczynski, 1998; Z. Chen & Wang, 2017). The basic logic behind the
 190 IBM method is that the fluid flow is simulated in the whole domain including the particles.
 191 For fluid inside a particle, a body force is inserted to make the fluid have the same rigid
 192 movement as the particle and the no-slip boundary condition is fulfilled for the external fluid
 193 flow. A fluid-solid interaction term Ω_i^{fs} is added in the standard LBM evolution equation.

$$f_i(\vec{x} + \vec{e}_i \delta t, t + \delta t) = f_i(\vec{x}, t) + (1 - B) \left\{ -\frac{\delta t}{\tau} (f_i - f_i^{eq}) \right\} + B \Omega_i^{fs}, \quad (17)$$

194 where B is a weighting parameter, which is a function of τ and the solid volume fraction γ :

$$B = \frac{\gamma(\tau/\delta t - 1/2)}{(1 - \gamma) + (\tau/\delta t - 1/2)}, \quad (18)$$

195 where γ is defined as the ratio of the solid volume over the lattice volume. When $\gamma = 0$, there
 196 are no solids in the corresponding fluid lattice. When $\gamma = 1$, the lattice is fully occupied
 197 by the solid phase. When $B = 0$, corresponding to $\gamma = 0$ (fluid lattice), the evolution
 198 equation degenerates to the standard one. Ω_i^{fs} can be obtained from a "bounce-back" of
 199 the nonequilibrium part of the density distribution:

$$\Omega_i^{fs} = f_{-i}(\vec{x}, t) - f_i(\vec{x}, t) + f_i^{eq}(\rho, \vec{u}_s) - f_{-i}^{eq}(\rho, \vec{u}_s), \quad (19)$$

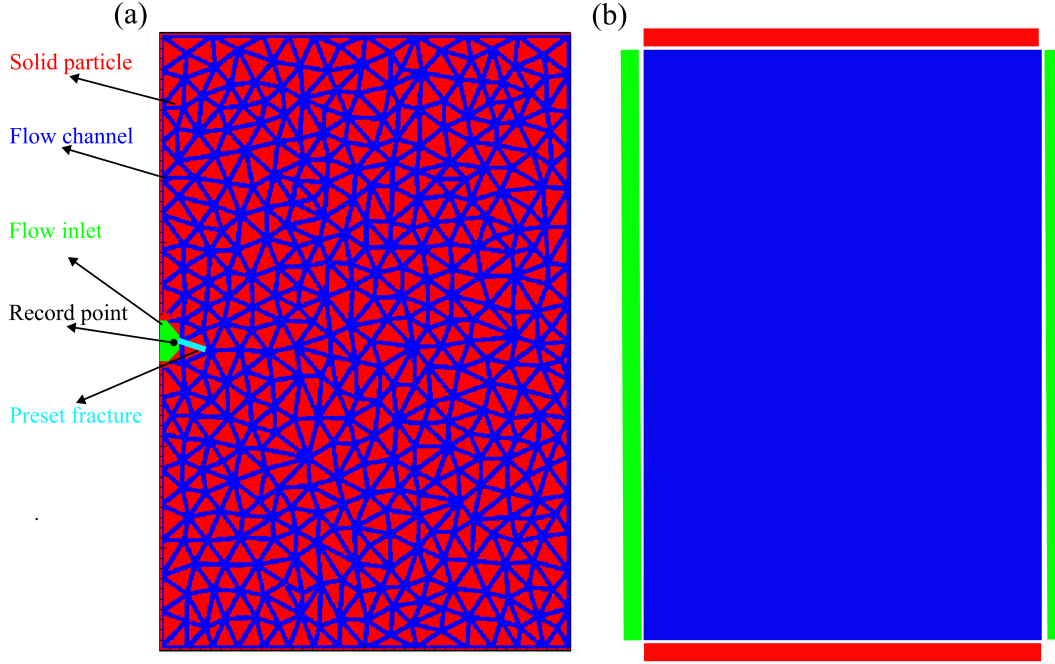
200 where f_{-i} refers to the "bounce-back" state from f_i by reversing all unit velocity vector,
 201 i.e. \vec{e}_i to $-\vec{e}_i$, and u_s is the velocity of the solid particle at time $t + \delta t$ at the position
 202 \vec{x} . To obtain the solid velocity, a force analysis of the particle is required. However, in
 203 this work, the particles are assumed to be unmovable to avoid the numerical error caused
 204 by particle vibrations. For cases with non-negligible particle velocities, Z. Chen and Wang
 205 (2020) proposed an improved IBM method, which incorporates the inertial force term with
 206 a finite-difference expression.

207 In Appendix A and Appendix B, a gravity-driven Poiseuille flow in a slit and a Brazilian
 208 test are used to validate the correctness of LBM and DEM schemes.

209 2.2 Simulation setup

213 The simulation model considered is a rectangular plate with a width of 4.0 cm, length
 214 of 6.0 cm, and thickness of 1.28 mm. The solid particles are shown in red in Fig. 1(a) with
 215 a total number of 741. The solid particles are eroded and dilated to form channels for the
 216 fluid flow (shown in blue in Fig. 1). The solid volume fraction γ is used to control the initial
 217 permeability of the flow domain in the LBM lattice. For the whole flow domain, there is a
 218 predefined γ controlling the initial permeability of the matrix, which can be used to mimic
 219 the leakage of injected fluid to formation in reality. A small cave on the left side is assigned
 220 as the fluid inlet and the initial γ value is zero. A preset fracture is denoted in Fig. 1(a),
 221 which mimics the perforation process in reality and helps to intrigue the hydraulic fracture.
 222 The detailed simulation parameters are listed in Table. 1.

223 Four rectangular plates on each side of the domain are added to implement differ-
 224 ent stresses on the horizontal (left-right) and vertical (top-bottom) directions, shown in



210 **Figure 1.** Calculation domain with a length of 6 cm, a width of 4 cm, and a thickness of 1.28
 211 mm

225 Fig. 1(b). The horizontal and vertical plates have a length of 4.0×10^{-2} m and 6.0×10^{-2}
 226 m. The width and height of plates are the same as the thickness of the particle, 1.28×10^{-3}
 227 m. There is a constant flow-rate condition for the inlet and a fixed pressure is assigned on
 228 the right side of the domain. All the other boundaries are set as solid.

229 Since the discrete element method is only conditionally stable, the time step should
 230 be small enough to reach the convergence. The critical time step is a function of the
 231 particle mass, its stiffness, and its arrangement (O’Sullivan & Bray, 2004). To ensure the
 232 convergence, the time step fulfills the criterion below (S. A. Galindo-Torres et al., 2012):

$$\Delta t_{critical} = 0.1 \sqrt{\frac{M_{min}}{C_{nmax} + B_{nmax}}}, \quad (20)$$

233 where M_{min} is the minimum mass of all particles, C_{nmax} and B_{nmax} are the maximum
 234 normal contact and bond stiffness of all particles, respectively. From Eq. 20, a larger value
 235 of the particle stiffness, a smaller time step is required. In this work, the heterogeneity of
 236 rock strengths is considered, which focuses more on the variations of rock strengths. Specific
 237 rock strengths are excluded as the influential factor. Therefore, we reduce the stiffness and
 238 modulus values to increase the time step as shown in Table. 1, which makes the simulation
 239 computationally affordable (Yousefi & Ng, 2017).

212

Table 1. Input parameters for the DEM-LBM simulation

| Parameter | Value |
|-------------------------------------|--|
| Normal contact stiffness, K_n | 1.0×10^6 N/m |
| Tangential contact stiffness, K_t | 1.0×10^6 N/m |
| Normal elastic modulus, B_n | 2.0×10^6 [Pa] |
| Tangential elastic modulus, B_t | 4.2×10^6 [Pa] |
| Bond strength, ϵ_{th} | 0.01 [-] |
| Fluid density, ρ_f^* | 1.0×10^3 [kg/m ³] |
| Lattice size in LBM, δ_x^* | 1.0×10^{-4} [m] |
| Time step in DEM/LBM, δ_t^* | 1.0×10^{-6} [s] |

240 If the bond strengths of all particles are the same, it will lead to a homogeneous rock
 241 sample. However, real rock samples are always heterogeneous because of different mineral
 242 compositions and cement materials. Therefore, the heterogeneous bond strengths are more
 243 appropriate for real rocks and it is one of the influential factors investigated in this work.
 244 The Weibull distribution is widely adopted to describe heterogeneous bond strengths for
 245 brittle rocks (Van Mier et al., 2002; Z. Chen & Wang, 2017; Pan et al., 2018; Z. Chen et
 246 al., 2020):

$$f(\epsilon_{th}) = \frac{m}{\epsilon_{th}^0} \left(\frac{\epsilon_{th}}{\epsilon_{th}^0}\right)^{m-1} \exp\left(-\left(\frac{\epsilon_{th}}{\epsilon_{th}^0}\right)^m\right), \quad (21)$$

247 where ϵ_{th}^0 is the average bond strength threshold and is set as 0.01 in this work. m is the
 248 shape parameter, describing the heterogeneity degree of the bond strength. An infinitely
 249 large m corresponds to a homogeneous structure, while a low value of m indicates a hetero-
 250 geneous structure.

251 The influential parameters investigated in this work also include the injection rate
 252 and in-situ stress states. To properly choose the injection rate and the stress levels, we
 253 conducted a Buckingham analysis (Buckingham, 1915) with the following steps and scaled
 254 our simulation parameters with parameters in actual experiments.

- 255 • Choose possible variables: tensile strength S , viscosity of fluid ν , particle size l ,
 256 injection rate q , fluid density ρ . In total, the number of variables is 5;
- 257 • Find variables with repeating units: particle size l , injection rate q , fluid density
 258 ρ . Therefore, the number of dimensions is 3 and the basis of fundamental units are

259 T (time), L (distance), and M (mass). Therefore, there should be two independent
 260 dimensionless parameters (π_1 and π_2) concerning fluid viscosity ν and tensile strength
 261 S .

- 262 • The first dimensionless parameter π_1 :

$$\pi_1 = \nu \times l^a \times q^b \times \rho^c \quad (22)$$

263 The unit of π_1 is:

$$[\pi_1] = \left[\frac{L^2}{T}\right] \times [L]^a \times \left[\frac{L^3}{T}\right]^b \times \left[\frac{M}{L^3}\right]^c \quad (23)$$

264 Since π_1 is dimensionless, we have:

$$\pi_1 = \frac{\nu \cdot l}{q}, \quad (24)$$

265 which is similar to the Reynolds number, if l is the characteristic length of the flow
 266 channel.

- 267 • The second dimensionless parameter π_2 :

$$\pi_2 = S \times l^a \times q^b \times \rho^c \quad (25)$$

268 The unit of π_2 is:

$$[\pi_2] = \left[\frac{M}{T^2 L}\right] \times [L]^a \times \left[\frac{L^3}{T}\right]^b \times \left[\frac{M}{L^3}\right]^c \quad (26)$$

269 Since π_2 is dimensionless, we have:

$$\pi_2 = \frac{Sl^4}{q^2 \rho} = \frac{S}{\rho q^2 / l^4}, \quad (27)$$

270 where the denominator part is equivalent to the dynamic pressure term $\frac{1}{2}\rho u^2$.

271 To estimate proper injection rates and stress levels, we take the experiment parameters
 272 from Liu et al. (2018), i.e. $q = 3.26 \times 10^{-7} \text{ m}^3/\text{s}$, $\nu = 6.7 \times 10^{-5} \text{ m}^2/\text{s}$, $S = 5.7 \times 10^6 \text{ Pa}$,
 273 and $\rho = 1000 \text{ kg/m}^3$. The particle size l is estimated as $5.0 \times 10^{-3} \text{ m}$ for the glutenite
 274 rock used in the experiment. On the simulation side, we choose the dynamic viscosity
 275 as $\nu_s = 5.0 \times 10^{-4} \text{ m}^2/\text{s}$ and fluid density as $\rho_s = 1000 \text{ kg/m}^3$. The particle size is esti-
 276 mated by $l_s = 0.25\sqrt{A_{\max}}$, where $A_{\max} = 5.0 \times 10^{-6} \text{ m}^2$ is the maximum particle area in
 277 the simulation. Correspondingly, the injection rate in the simulation is estimated from π_1 ,
 278 $q_s = 2.72 \times 10^{-7} \text{ m}^3/\text{s}$, and the corresponding injection velocity is $u_s = 0.34 \text{ m/s}$. From
 279 π_2 , the proper magnitude of tensile strength can be estimated. Please note that the tensile
 280 strength in the simulation should be scaled according to the elastic modulus and failure
 281 criterion. As a result, a stress magnitude of 10 MPa in the experiment corresponds to

282 1.68×10^4 Pa in the simulation. In this way, proper values of injection rates and stress
 283 levels are found for the simulation with an appropriate magnitude.

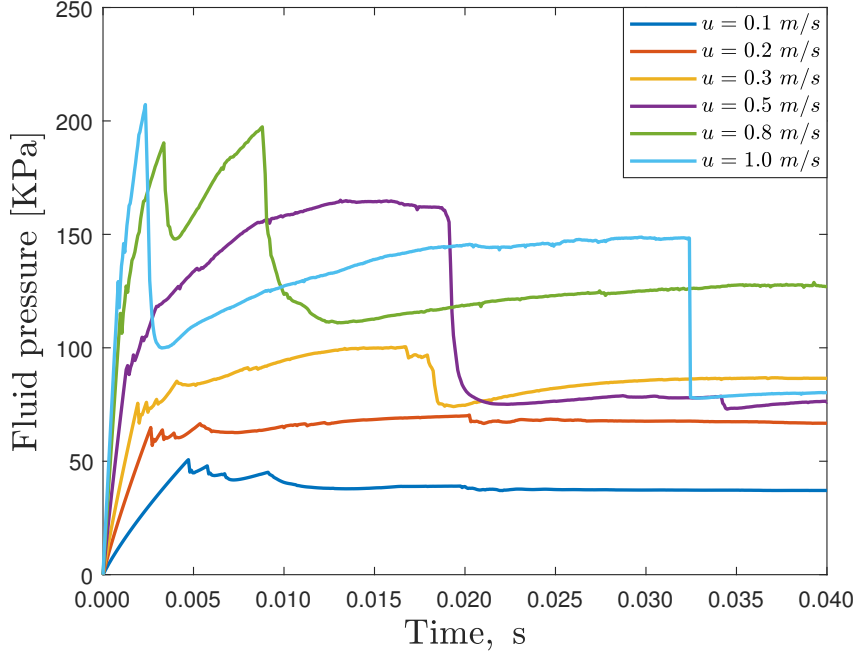
284 **3 Results**

285 We systematically investigate the individual impact of injection rates, fluid viscosity,
 286 in-situ stresses, heterogeneous bond strengths, and formation permeability on fracture ini-
 287 tiation and propagation. Each influential factor is evaluated with the other factors fixed at
 288 a reference value. The reference value for each parameter is listed as follows: 0.2 m/s for
 289 the injection velocity, 5.0×10^{-4} m²/s for the fluid kinematic viscosity, no stress state for
 290 the in-situ stress states, homogeneous bond strengths for heterogeneous bond strengths and
 291 a solid volume fraction of 0.97 for the formation permeability.

292 **3.1 Impact of injection rate**

293 Six different injection velocities are chosen for the investigation under an unconfined
 294 condition: 0.1 m/s, 0.2 m/s, 0.3 m/s, 0.5 m/s, 0.8 m/s and 1.0 m/s. The pore pressure
 295 variations of the inlet position (the record point shown in Fig. 1a) are shown in Fig. 2.
 296 With injection velocity increases, the fracture initiation pressure also increases, consistent
 297 with many observations from lab experiments and numerical simulation (Morgan et al., 2017;
 298 Zhuang et al., 2019; Duan et al., 2018). For low injection velocities ($u = 0.1$ and 0.2 m/s),
 299 the pore pressure vibrates, but decreases with fracture propagation, which indicates that
 300 the fracture volume and leak-off volume expand at a roughly equal or a slightly greater
 301 rate than the injection rate. For high injection velocities ($u > 0.2$ m/s), the pore pressure
 302 continues to increase after the fracture initiation, indicating that the fracture volume and
 303 leak-off volume increase at a smaller rate than the injection rate.
 304

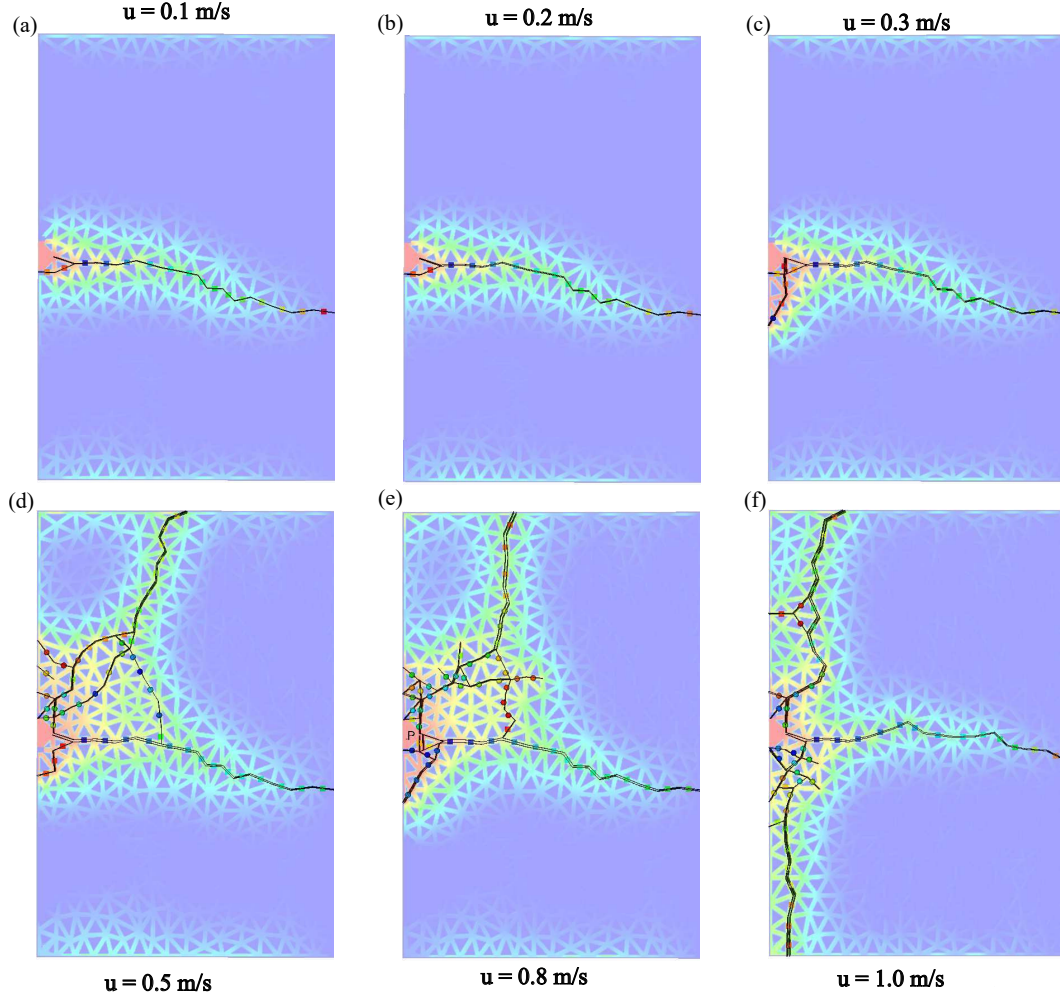
305 The fracture geometries of each case are shown in Fig. 3 with the fluid pressure dis-
 306 tribution shown in the background. The center point of each fracture is represented by a
 307 solid square for a tensile fracture and a circle for a shear fracture. The color variations from
 308 cold (blue) to warm (red) refer to the sequence of generation. For low injection velocity,
 309 the fracture geometries are almost the same (Fig. 3(a,b)). However, with the increasing
 310 injection velocities, the fracture geometries become complex with branches. The main hori-
 311 zontal fractures in different cases are similar. However, when the horizontal fracture reaches
 312 the right boundary, vertical fractures tend to form at a high injection velocity and most
 313
 314
 315
 316



293 **Figure 2.** The pore pressure evolution at the record point for cases with different injection rates

317 fractures generated in the transition zones (from horizontal to vertical) are shear instead
 318 of tensile fractures. When the horizontal fracture reaches the right boundary, the pore
 319 pressure in the hydraulic fracture compresses the sample in the top-bottom direction. The
 320 stress condition makes the newly generated fracture perpendicular to the horizontal fracture
 321 because the fracture trace should be perpendicular to the minimum principle stress (zero
 322 stress in the left-right direction). In addition, when the injection velocity is high, the pore
 323 pressure becomes significantly high as shown in Fig. 2, which is large enough to generate a
 324 new fracture in the top-bottom direction.

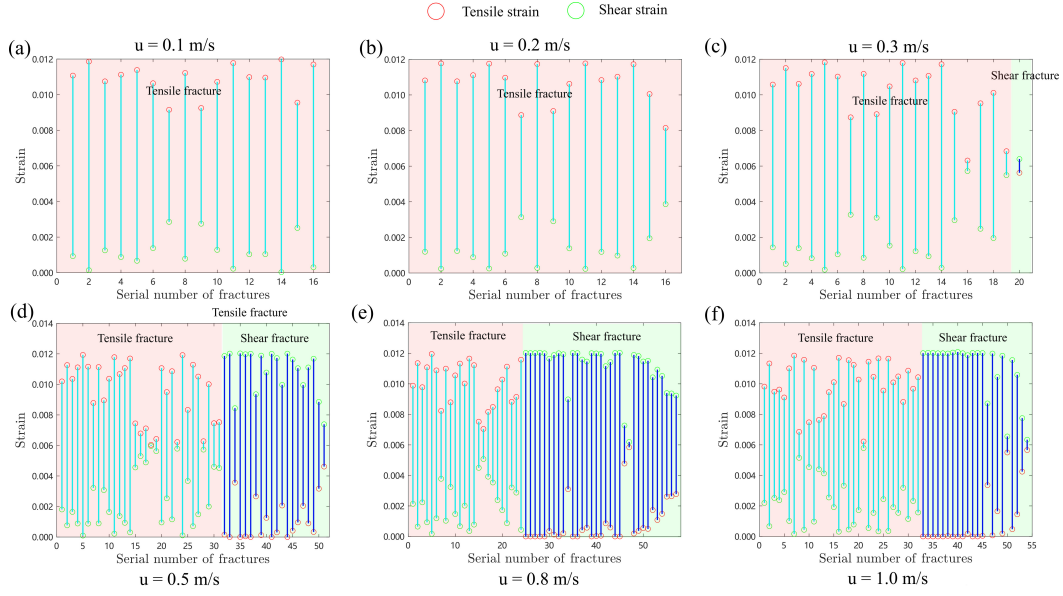
326 Fig. 4 shows the tensile and shear strain component of each fracture segment in Fig. 3.
 327 The tensile and shear strains are represented with red and green circles, respectively. The
 328 links between tensile and shear strain for tensile and shear fractures are light blue and
 329 regular blue. When the injection rate is small, all fractures are tensile fractures with in-
 330 significant shear strain between particles. However, when the injection rate increases, more
 331 fractures have a comparable even larger shear strain than tensile strain. The proportion of
 332 shear fractures increases with the increasing injection velocity, which is consistent with the
 333 observation in Duan et al. (2018).



305 **Figure 3.** Fracture geometries of cases with different injection rates at 0.04s. The background
 306 shows the fluid pressure distribution in the entire domain. The center of each fracture segment is
 307 marked with squares for tensile fractures and circles for shear fractures. The color variations from
 308 blue to red refer to the generation sequence of each type of fractures.

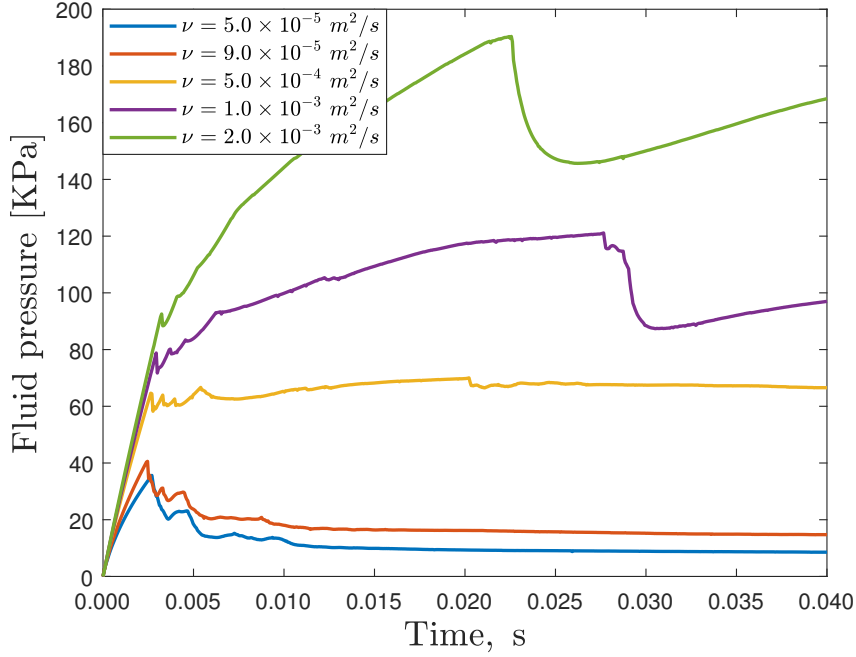
334 3.2 Impact of fluid viscosity

340 Six levels of viscosity are chosen for the investigation under an unconfined condition:
 341 $\nu = 5.0 \times 10^{-5} \text{ m}^2/\text{s}$, $9.0 \times 10^{-5} \text{ m}^2/\text{s}$, $2.0 \times 10^{-4} \text{ m}^2/\text{s}$, $5.0 \times 10^{-4} \text{ m}^2/\text{s}$, $1.0 \times 10^{-3} \text{ m}^2/\text{s}$,
 342 $2.0 \times 10^{-3} \text{ m}^2/\text{s}$. The pore pressure variations at the record point are shown in Fig 5. With
 343 viscosity increases, the initial stage of the pressure build-up of all cases is similar, but the
 344 initiation pressure increases for the case with a high viscosity. Similar results are observed
 345 in Duan et al. (2018) and Z. Chen et al. (2020). The fracture geometries are similar for
 346 different fluid viscosity and three examples are presented in Fig. 6. When the viscosity is



325

Figure 4. Tensile and shear strain of each fracture segment in Fig. 3



335

Figure 5. The pore pressure evolution at the record point for cases with different fluid viscosity

347

low, the fluid can leak into the formation easily and make the pore pressure of the formation

348

increase as shown in Fig.6(a). Also, a few branches along the main hydraulic fracture can be

349

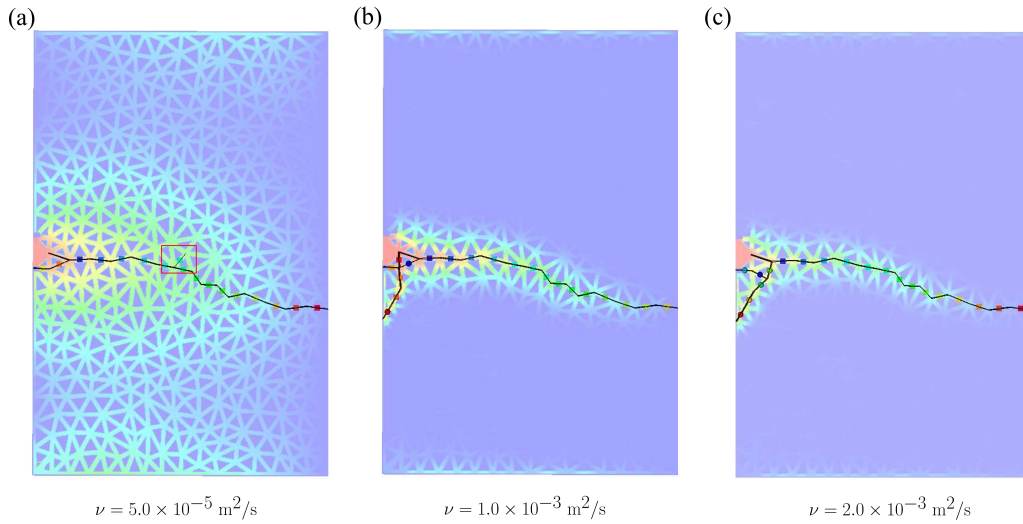
observed in Fig. 6(a). For high-viscosity fluid, the pore pressure can only propagate to the

350

neighboring region and the region area shrinks with increasing viscosity. In addition, after

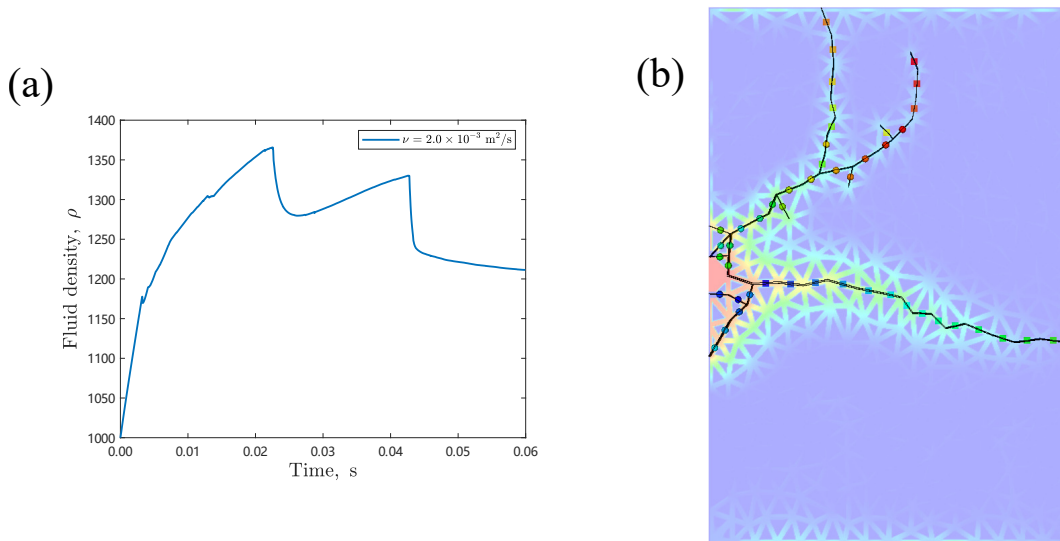
351

the horizontal fracture reaches the right boundary, new fractures can be generated at the



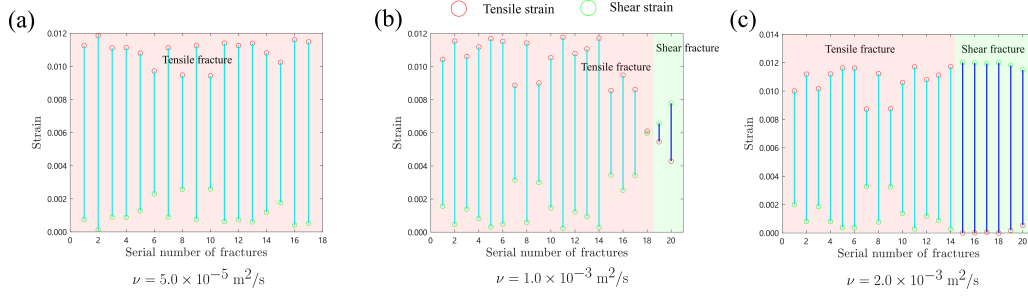
336 **Figure 6.** Fracture geometries of cases with different fluid viscosity at 0.04s. A branch generated
 337 in the low-viscosity case is marked in the red box.

352 inlet because of the high pore pressure therein as shown in Fig. 5. For the highest viscosity
 353 considered in this work, $\nu = 2.0 \times 10^{-3} \text{ m}^2/\text{s}$, the pore pressure continues to increase after
 354 0.04 s as shown in Fig. 7(a). New fractures are generated in the vertical direction and
 355 continue to propagate as shown in Fig. 7(b). Most inclined fractures are shear fractures and
 the fractures become tensile in a perpendicular direction.



338 **Figure 7.** The pore pressure evolution at the record point for cases with high fluid viscosity,
 339 $\nu = 2.0 \times 10^{-3} \text{ m}^2/\text{s}$ (a) and the corresponding fracture geometries (b) at 0.06s.

357 Fig. 8 presents the strain component of each fracture segment in Fig. 6. When the
 358 viscosity is low, all generated fractures are tensile fractures. With the increasing viscosity,
 359 the shear strain becomes more significant and the proportion of shear fractures also increases.
 360 However, the main horizontal fractures are mostly tensile and shear fractures are usually
 the newly generated inclined fractures.



356 **Figure 8.** Tensile and shear strain of each fracture segment in Fig. 6

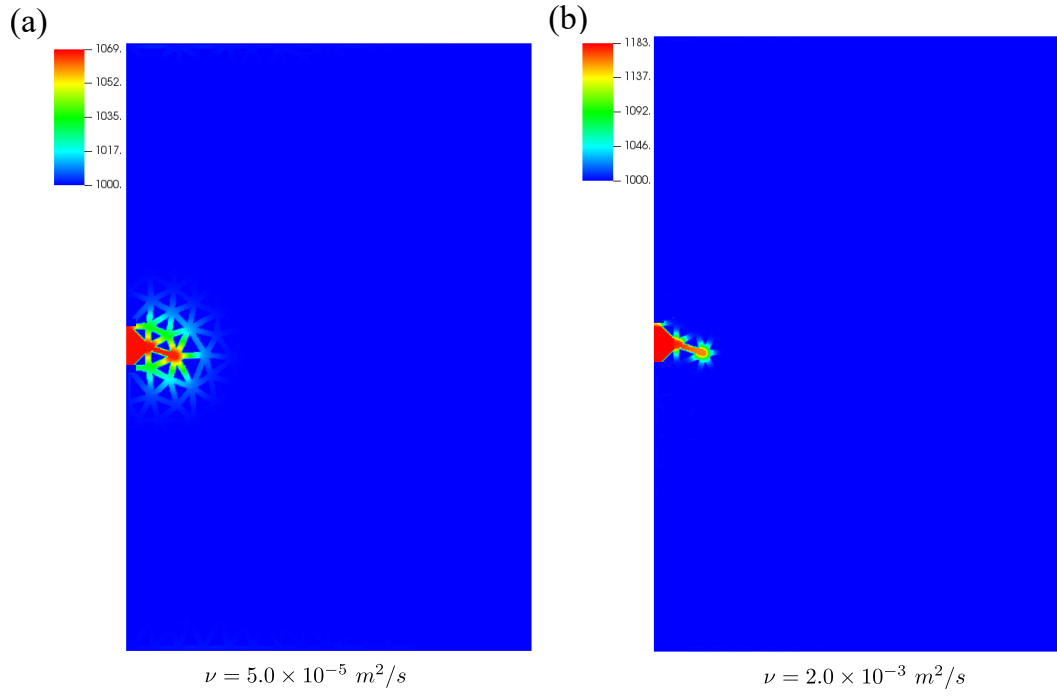
361

362 Fluid with low viscosity has stronger penetration capability than highly viscous fluid.
 363 Fig. 9 shows the pressure distribution of cases with low and high fluid viscosity at the fracture
 364 initiation stage. The pressure propagates much farther in the low-viscosity case. Similar
 365 observations are obtained from Duan et al. (2018) and Z. Chen et al. (2020). The penetration
 366 capability may not change the fracture geometries significantly in the homogeneous media
 367 since all bonds are equally strong. However, for heterogeneous media or formations with
 368 preexisting natural fractures, such penetration capability can help to generate more complex
 369 fracture geometries (Z. Chen et al., 2020).

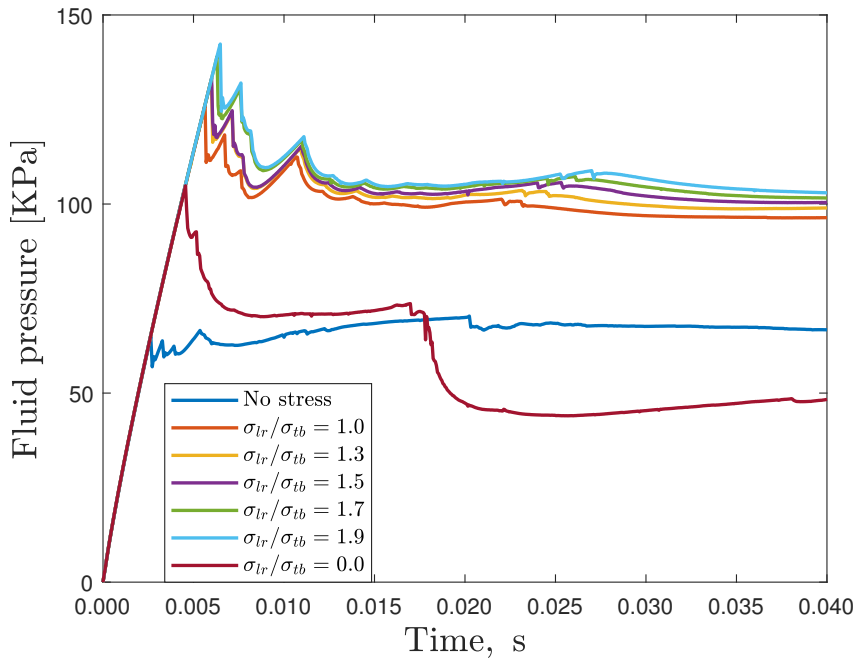
372 3.3 Impact of in-situ stress states

373 The stress on the top-bottom direction is fixed at 1.68×10^4 Pa as derived in Section. 2.
 374 Different stress anisotropy degrees are represented by the stress ratio between σ_{lr} (left-
 375 right direction) and σ_{tb} (top-bottom direction). Six levels of the ratio are chosen for the
 376 investigation: $\sigma_{lr}/\sigma_{tb} = 1.0, 1.3, 1.5, 1.7, 1.9, 0$.

380 The pore pressure variations of each case at the record point are shown in Fig. 10,
 381 where the initiation pressure increases due to the imposed in-situ stresses. A larger imposed
 382 in-situ stress leads to a higher fracture initiation pressure. However, the implementation of

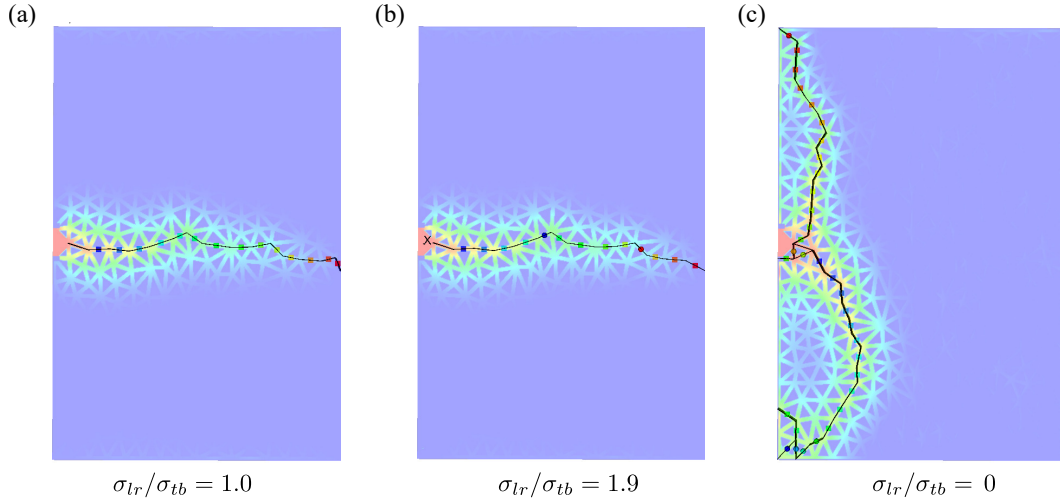


370 **Figure 9.** Pore pressure distribution at the fracture initiation stage for cases with a low(a) and
 371 high (b) fluid viscosity, respectively



377 **Figure 10.** The pore pressure evolution at the record point for cases with different in-situ stress
 378 states

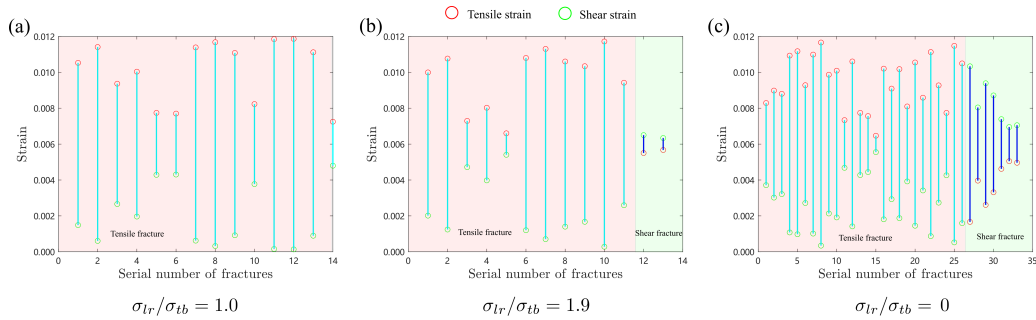
383 in-situ stress does not change the fracture geometry significantly. For the first five cases,
 384 where σ_{lr} is the maximum principle stress, the fracture geometries are similar and have
 385 a direction perpendicular to the minimum stress direction (top-bottom direction). Two
 386 examples of with $\sigma_{lr}/\sigma_{tb} = 1.0$ and 1.9 as shown in Fig. 11(a and b). For the case where no
 387 stress applies in the left-right direction, the fracture propagates in the top-bottom direction
 388 as expected, which is perpendicular to the minimum principle stress (left-right direction has
 no stress).



379 **Figure 11.** Fracture geometries of cases with different in-situ stress states at 0.04s

389

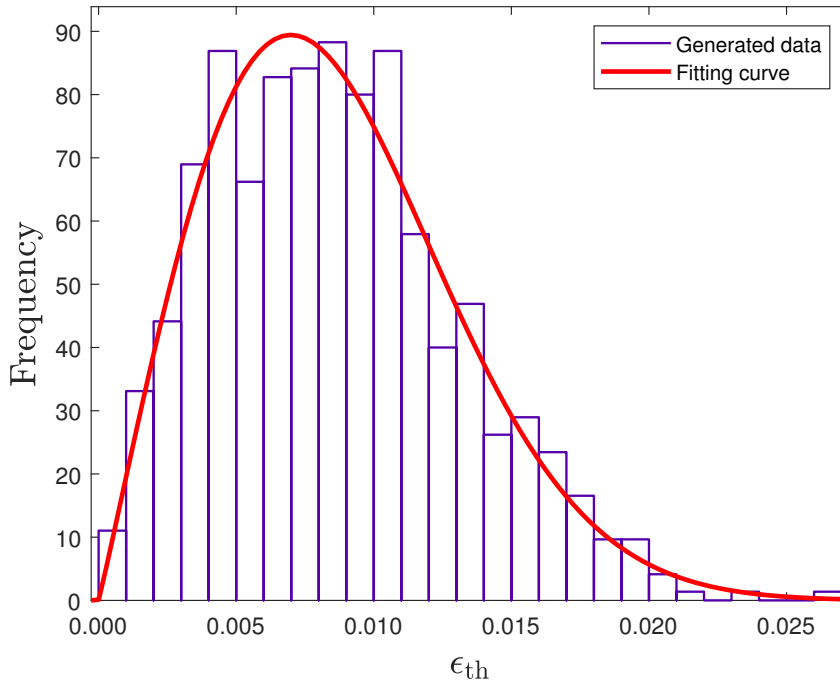
391 Fig. 12 shows the tensile and shear strain of each generated fracture in Fig. 11. The
 392 fractures are dominated by tensile fractures, but the shear fractures tend to increase with
 393 the anisotropy level. In addition, compared with the cases with no stress imposed (Fig. 4a),
 several tensile fractures have significant shear strain components.



390 **Figure 12.** Tensile and shear strain of each fracture segment in Fig. 11

394 **3.4 Impact of heterogeneous bond strengths**

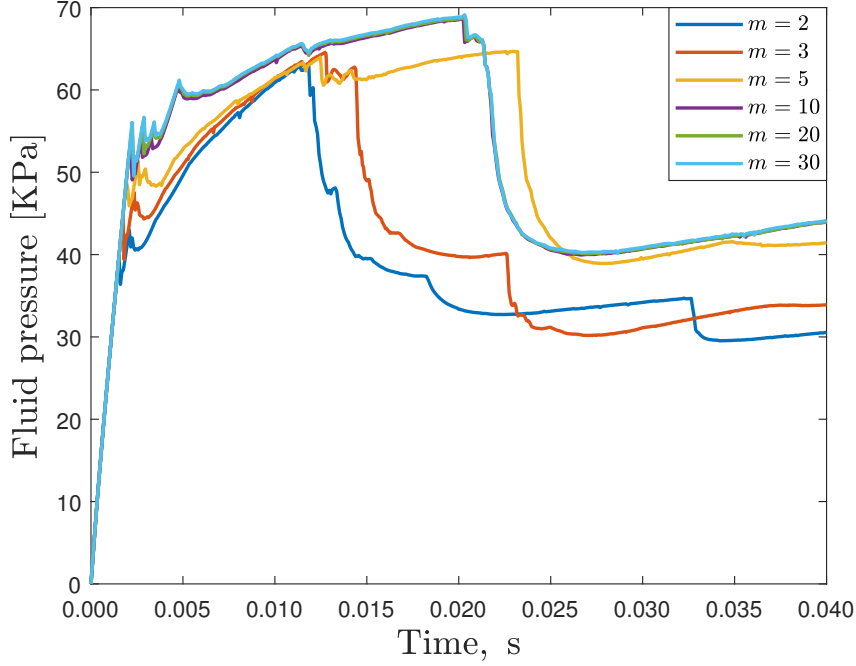
396 To investigate the heterogeneous characteristic of natural rocks, we choose different
 397 values of m in the Weibull distribution to make the bond strength vary. The average bond
 398 strength is 0.01 and six values of m are chosen for the consideration: $m = 2, 3, 5, 10, 20, 30$,
 399 A smaller m value represents a higher heterogeneity degree. For the case with $m = 2$, the
 400 strength distribution and the fitting curve are shown in Fig. 13. The fitting parameters are
 401 0.0097 for the mean and 2.04 for the shape factor, m . Therefore, the chosen quantity of
 402 particles (741) is sufficient to recover the prescribed distribution for the heterogeneous bond
 strengths.



395 **Figure 13.** A Weibull distribution fitting of heterogeneous bond strengths

403

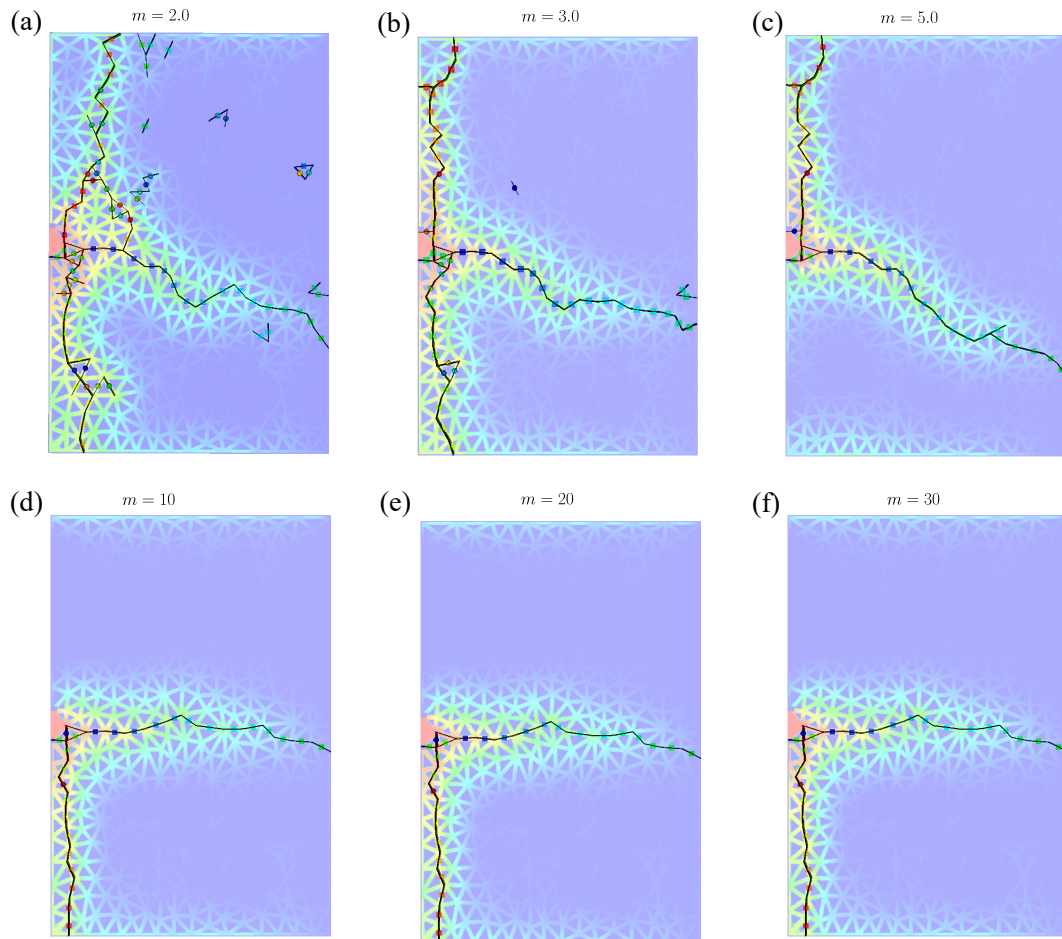
406 The pore pressure variations of each case at the record point are shown in Fig. 14. The
 407 pressure buildup process is the same for all cases with different heterogeneity. However, the
 408 initiation pressure is higher for cases with more homogeneous levels. The most heterogeneous
 409 case, where $m = 2.0$, has the lowest initiation pressure.



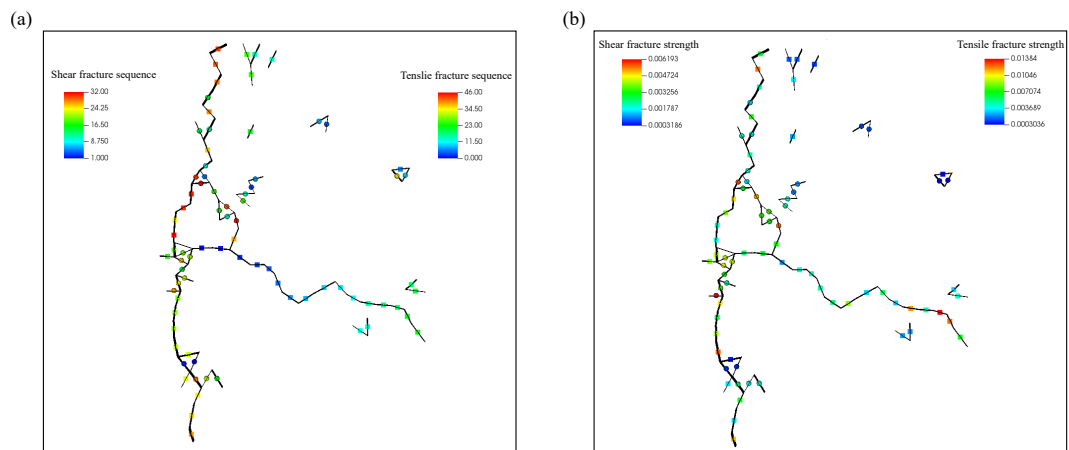
404 **Figure 14.** The pore pressure evolution at the record point for cases with different heterogeneity
 405 degrees of bond strengths

412 The fracture geometries of each case are shown in Fig. 15. The higher the heterogeneity
 413 degree is, the more complex the fracture geometry is. For the case with $m = 2.0$, the frac-
 414 ture geometries are the most complex with several branches. There are also some fractures
 415 disconnected from the main fractures, which are caused by the leakage of fluid into the
 416 matrix. To better demonstrate this process, the fracture traces are plotted with the bond
 417 strength and generation sequence marked in Fig. 16. Most disconnected fractures are shear
 418 fractures and their bond strengths are quite low as shown in Fig. 16(b). For the disconnected
 419 fractures, the leakage of injected fluid can enhance the pore pressure therein and the high
 420 pressure in the main hydraulic fracture can increase the local principal stresses. The in-
 421 creased principal stresses usually stifle possible microseismicity from occurring as concluded
 422 in N. R. Warpinski et al. (2001) and Zhu et al. (2022). However, there are no initial stresses
 423 applied in this simulation, therefore, the increase of principle stresses and pore pressure can
 424 trigger the shear failure or even tensile failure of those weak bonds.

428 For more homogeneous cases, where m is large, the fracture geometries do not change
 429 significantly. However, compared with a completely homogeneous case (Fig. 3a), there are
 430 two main fracture traces instead of a single horizontal one. This fracture geometry is similar

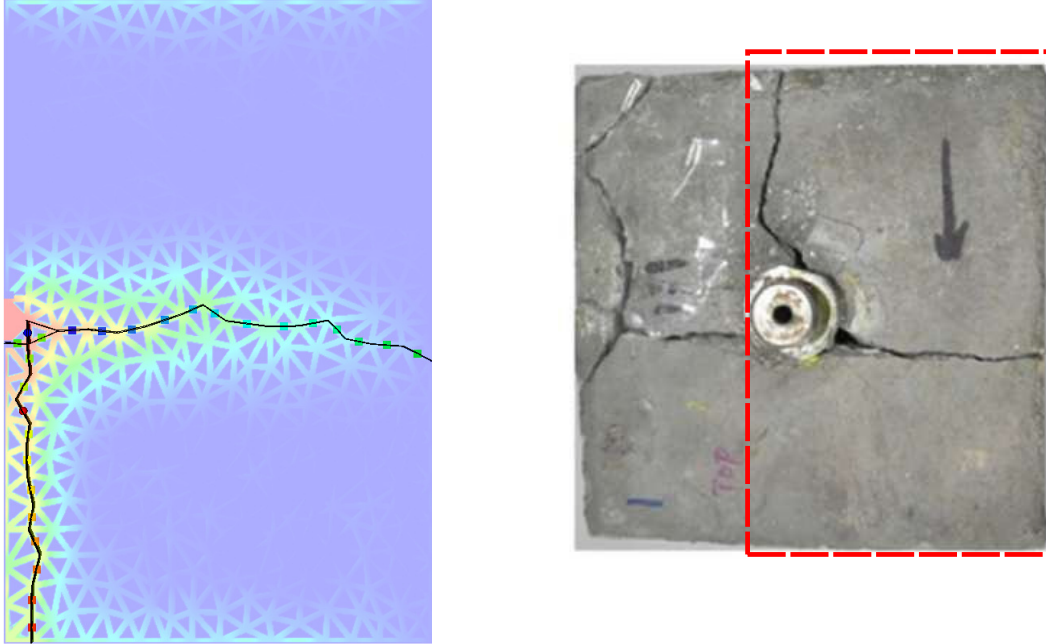


410 **Figure 15.** Fracture geometries of cases with different heterogeneity degrees of bond strengths
 411 at 0.04s



425 **Figure 16.** The generation sequence (a) and bond strength (b) of each fracture segment

431 to the experiment results in Liu et al. (2018) as shown in Fig. 17 since the actual rocks are
 432 not completely homogeneous. Similar patterns do support the correctness of the numerical
 method in this work.



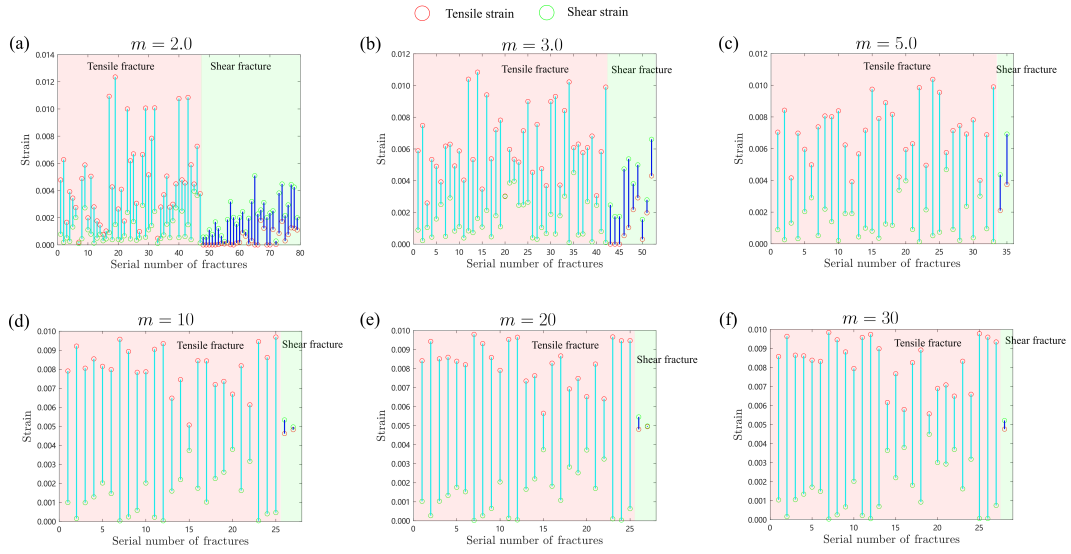
426 **Figure 17.** A comparison of fracture geometries with results in a lab experiment (Liu et al.,
 427 2016)

433

434 The strain components of each fracture in Fig. 15 are shown in Fig. 18. For highly
 435 heterogeneous cases, many shear fractures are generated. For the most heterogeneous case,
 436 32 out of 78 fractures are shear fractures, corresponding to a proportion of 41%. With
 437 the heterogeneity degree decreases, the proportion of shear fractures decreases sharply and
 438 tensile fractures are dominated.

440 **3.5 Impact of formation permeability**

441 The solid volume fraction (γ) has a negative correlation with the formation perme-
 442 ability. A larger γ indicates that more voids are occupied by impermeable solids and the
 443 corresponding formation permeability is lower. Impacts of different values of solid volume
 444 fractions (γ) are evaluated and six values are chosen: $\gamma = 0.85, 0.9, 0.92, 0.95, 0.97, 0.99$.

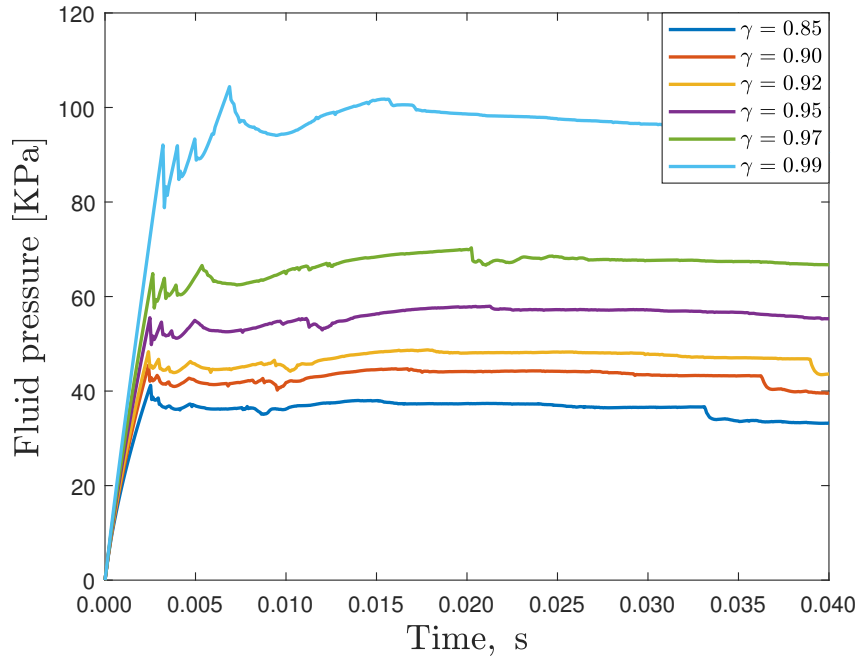


439

Figure 18. Tensile and shear strain of each fracture segment in Fig. 15

448

The pore pressure variations at the record point for different cases are shown in Fig. 19. The pressure evolution curves have similar shapes. The lower the matrix permeability, the



445

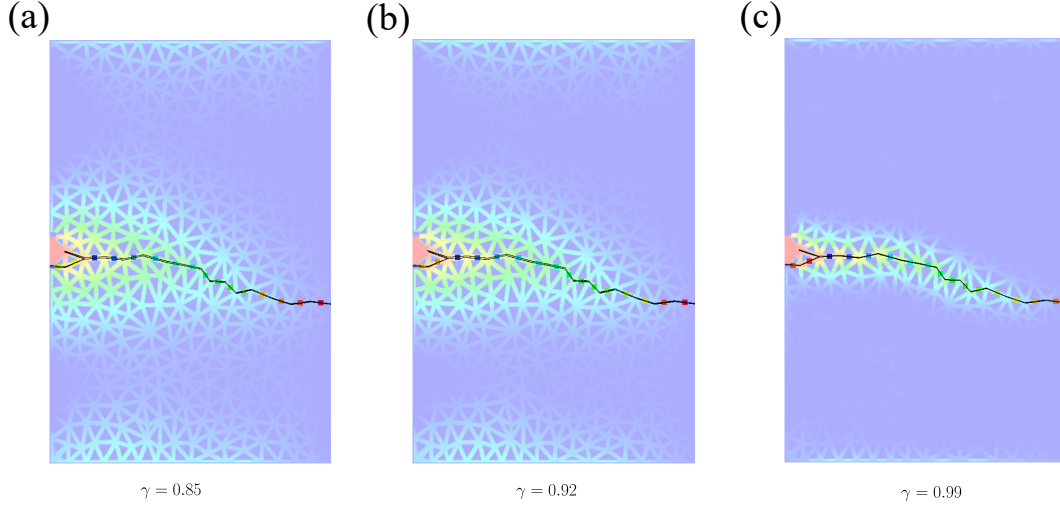
Figure 19. The pore pressure evolution at the record point for cases with different matrix permeability

449

450

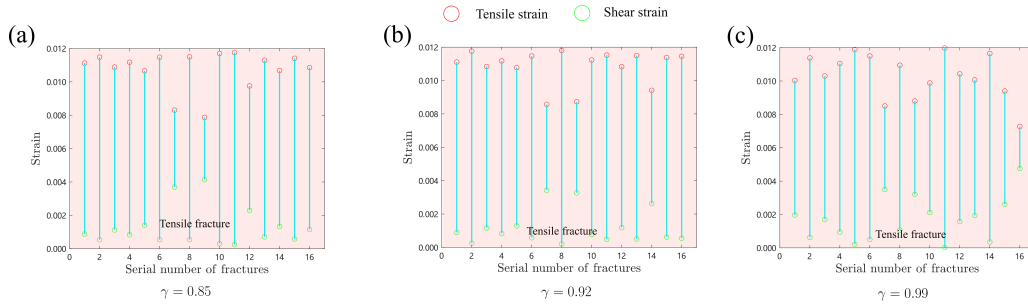
higher the fracture initiation pressure is, which is consistent with the observations in the

451 lab experiments (Fazio et al., 2021). The fracture geometries are similar for all cases,
 452 which are horizontal. Three examples with $\gamma = 0.85, 0.92$ and 0.99 are shown in Fig. 20.
 453 The corresponding strain components of each fracture are shown in Fig. 21. All generated
 fractures are tensile fractures with insignificant shear strain.



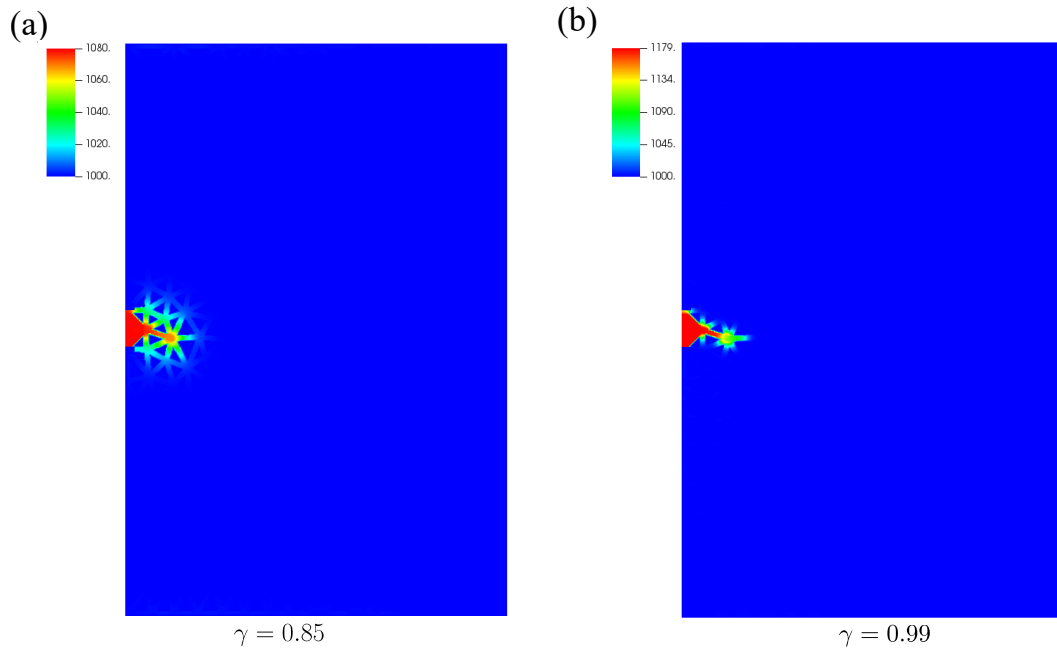
447 **Figure 20.** Fracture geometries of cases with different formation permeability at 0.04s

454



455 **Figure 21.** Tensile and shear strain of each fracture segment in Fig. 20

458 The matrix permeability controls the leakage of fluid as shown in Fig. 20. The pressure
 459 propagates to a larger region in a highly permeable case (Fig. 20a) and the influential region
 460 is quite narrow for the weakly permeability cases (Fig. 20c). To better demonstrate this
 461 phenomenon, the pressure distributions at the fracture initiation of the case with $\gamma = 0.85$
 462 and $\gamma = 0.99$ are shown in Fig. 22. For the case with $\gamma = 0.99$, the pore pressure is quite
 463 high in the cave and the preset fracture but hardly propagates to the neighboring region.
 464 For the case with $\gamma = 0.85$, the pressure propagates to a much larger region.



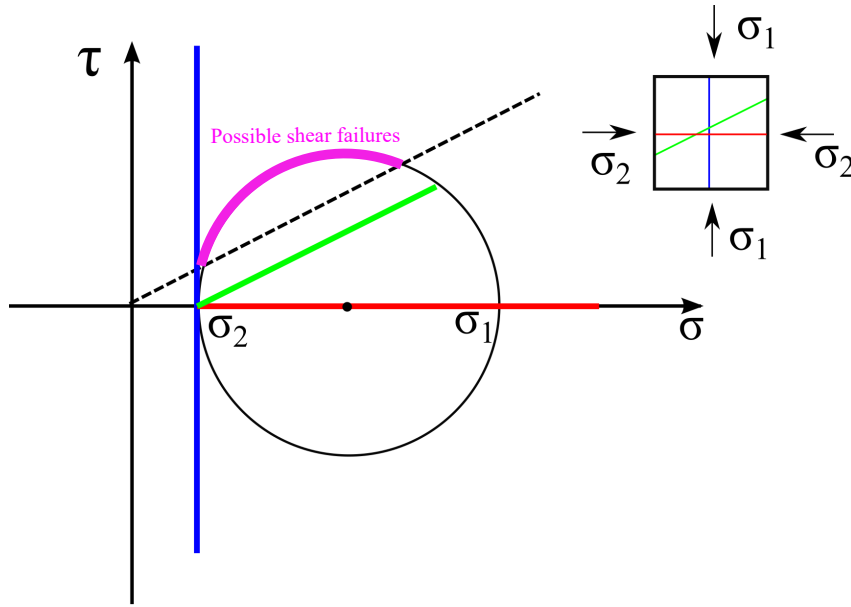
456 **Figure 22.** Pore pressure distribution at the fracture initiation stage for cases with a high (a)
 457 and low (b) formation permeability, respectability

465 4 Discussions

466 In this work, we conducted a systematical analysis of the impacts of different factors
 467 (formation parameters, treatment parameters, and rock properties) on the fracture initiation
 468 and propagation process. The impact of each factor is evaluated with the other factors fixed.
 469 It is beneficial to first have an independent factor analysis and provide a comprehensive and
 470 detailed understanding of each factor. Subsequently, analysis of coupled effects or impacts
 471 of interactions between different factors can be extended, which is technically available with
 472 the foundation constructed in this work. In addition, with optimization of the algorithm
 473 efficiency and development of new modulus, more factors, such as temperature, grain size,
 474 different injection schemes, can be considered in the future for more complex scenarios.

475 Most primary hydraulic fractures (horizontal ones in most cases) are tensile fractures.
 476 However, when the primary fracture reaches the right boundary, vertical tensile fractures
 477 are possible if the pore pressure is high enough. In the transition zone, shear fractures
 478 are more dominant than tensile fractures, like Fig. 3(d-f), Fig. 7(b), and Fig. 15(a-c). The
 479 generated shear fractures are usually inclined and a Mohr's circle analysis may explain this
 480 phenomenon. In Fig. 23, a Mohr's circle and stress states of three planes (blue, green, and

481 red) are determined by the intersection point between the plane and the Mohr's circle. For
 482 the demonstration purpose, the friction coefficient is 0.4 and the cohesion strength is set to
 483 zero. The specific Mohr's circle in the simulation domain is caused by the enhanced pore
 484 pressure from leak-off and principle stresses generated by the compression from the primary
 485 hydraulic fracture. The purple arc in Morh's circle refers to all possible plane directions
 486 that can trigger a shear failure. The inclined bonds are more likely to form shear failures
 487 because their orientations fall into the shear failure range.



488 **Figure 23.** A sketch map of a Mohr's circle for different fracture planes (red, blue, and green)

489 The DEM-LBM coupled method is powerful to investigate the detailed fracture initia-
 490 tion and propagation process. However, there are still several limitations and two important
 491 ones are listed below:

- 492 • The roughness of the fracture surface is difficult to be reproduced with DEM since
 493 there are large differences in scales between the particle size and asperity size. There-
 494 fore the shear dilation process is hard to mimic, which is also an important mechanism
 495 to form complex fracture networks in a hydraulic fracturing process (Rahman et al.,
 496 2002).
- 497 • The breakage of particles is not applicable in this DEM scheme. Therefore, only
 498 breakage between particles is possible. However, several experiments observed that

499 hydraulic fractures can cut the minerals and propagate across particles, especially in
500 hydraulic fracturing with critical CO₂ (Y. Chen et al., 2015),

501 Therefore, improvements in the numerical scheme or the development of new schemes are
502 still necessary to simulate the hydraulic fracturing process in reality.

503 **5 Conclusions**

504 In this work, a comprehensive investigation of the influential factors on the initiation
505 and propagation in a hydraulic fracturing process is conducted with the DEM-LBM method.
506 The factors include formation parameters (in-situ stress states), treatment parameters
507 (injection rates and fluid viscosity), and rock properties (heterogeneity of rock strengths
508 and formation permeability). Several important findings and conclusions are drawn below:

- 509 • All factors have a significant impact on the fracture initiation pressure. A higher
510 injection rate, higher viscosity, and larger in-situ stress will increase the initiation
511 pressure, while a higher formation permeability and higher heterogeneity degree of
512 bond strengths will decrease the initiation pressure.
- 513 • Injection rate and heterogeneity degree have much significant impact on the com-
514 plexity of generated fractures. Fluid viscosity, in-situ stress states, and formation
515 permeability do not change the geometrical complexity.
- 516 • Hydraulic fractures are usually tensile fractures, however, they usually do not have
517 pure tensile displacement. Shear fractures are possible and the shear displacement
518 can be significant under certain conditions, such as a high injection rate, and high
519 heterogeneity degrees.

520 **Acknowledgments**

521 This project was supported by the National Key Research and Development Program of
522 China (No. 2019YFA0708704). The authors would like to thank all editors and anonymous
523 reviewers for their comments and suggestions.

524 **Data Availability Statement**

525 The numerical simulation in this work is based on the open-source multi-physics simu-
 526 lation library MECHSYS developed by Dr. S.A. Galindo Torres. The library is available at
 527 <https://mechsys.nongnu.org/>.

528 **Appendix A Benchmark case for LBM simulation**

529 The Poiseuille flow in a slit driven by gravity is chosen as the benchmark case to
 530 validate the LBM algorithm. The slit has lengths and widths of 100 and 48 lattice units
 531 (lu). A bounce-back boundary condition is implemented on the top and bottom walls. A
 532 periodic boundary condition is adopted to avoid the entry or exit effect for the left and right
 533 boundaries.

534 The Reynolds number is 20 to ensure a laminar flow state. The maximum velocity
 535 (u_{max}) is chosen as $0.1 lu ts^{-1}$. The relaxation time (τ) is 1.0 for the simple bounce-
 536 back boundaries, which yield a kinematic viscosity (ν) of $1/6 lu^2 ts^{-1}$. Fluid density (ρ)
 537 is chosen as 1.0. The analytical solution for the gravity-driven Poiseuille flow yields a
 538 parabolic velocity profile:

$$u(x) = \frac{\rho g}{2\mu}(a^2 - x^2), \quad (A1)$$

539 where $u(x)$ is the velocity in the Y direction, a is the half width of the slit, g is the gravi-
 540 tational acceleration. The maximum velocity is :

$$u_{max} = \frac{\rho g a^2}{2\mu} \quad (A2)$$

541 Through rearranging Eq. A2, the corresponding gravitational acceleration (g) to drive the
 542 flow is calculated:

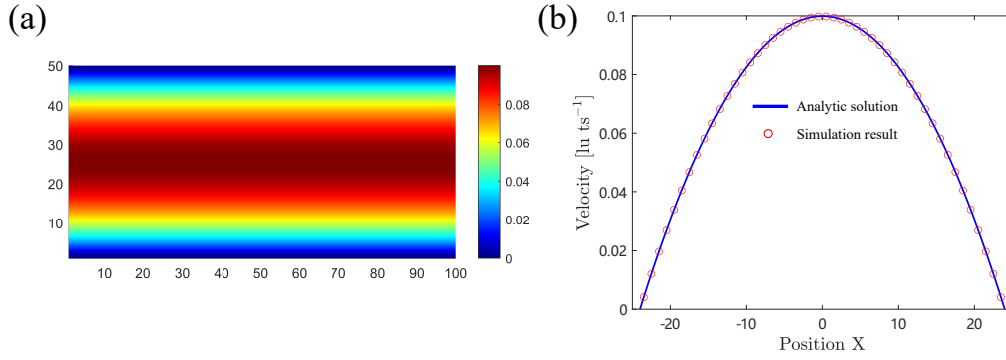
$$g = \frac{2\nu u_{max}}{a^2} \quad (A3)$$

543 Therefore, g is $5.7804 \times 10^{-5} lu ts^{-2}$.

546 The velocity distribution in the slit is shown in Fig. A1(a) and Fig. A1(b) shows the
 547 comparison between the analytical solution and the simulation result.

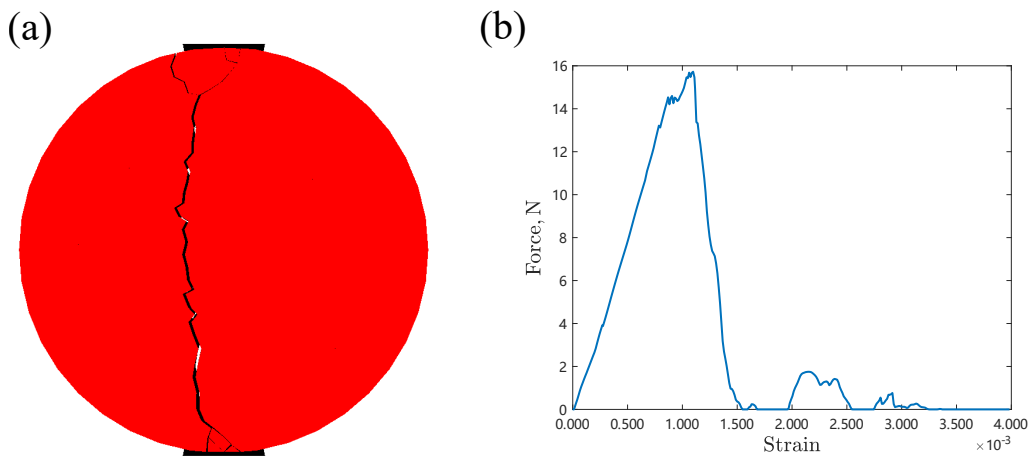
548 **Appendix B Benchmark case for the DEM simulation**

549 A Brazilian test is used to validate the correctness of the DEM simulation. A round
 550 disc with a diameter of 0.2 m and a thickness of 0.1 m is generated for the simulation. The



544 **Figure A1.** (a) The velocity distribution in a slit (b) Comparison between the analytical solution
 545 and LBM result

551 total number of particles is 1,924. The specific rock properties are not used in the simu-
 552 lation considering the computational cost. The normal and tangential contact stiffness are
 553 $1.0 \times 10^5 \text{N/m}$. The normal and tangential elastic modulus are $1.0 \times 10^5 \text{Pa}$. The threshold
 554 value on the total strain is 0.02. The time step is chosen as $4.5 \times 10^{-5} \text{s}$. The breaking results
 555 after the compression are shown in Fig. B1. A vertical fracture and V-shaped damage zones
 556 are observed, and similar results are found in lab experiments (Gong et al., 2019).



557 **Figure B1.** (a) Fractures formed after compression in a Brazilian test (b) The force-strain
 558 relation of the Brazilian test

References

- 559
- 560 Buckingham, E. (1915). The principle of similitude. *Nature*, *96*(2406), 396–397.
- 561 Chen, H., Meng, X., Niu, F., Tang, Y., Yin, C., & Wu, F. (2018). Microseismic monitoring
562 of stimulating shale gas reservoir in sw china: 2. spatial clustering controlled by the
563 preexisting faults and fractures. *Journal of Geophysical Research: Solid Earth*, *123*(2),
564 1659–1672.
- 565 Chen, S., & Doolen, G. D. (1998). Lattice boltzmann method for fluid flows. *Annual review*
566 *of fluid mechanics*, *30*(1), 329–364.
- 567 Chen, Y., Nagaya, Y., & Ishida, T. (2015). Observations of fractures induced by hydraulic
568 fracturing in anisotropic granite. *Rock Mechanics and Rock Engineering*, *48*(4), 1455–
569 1461.
- 570 Chen, Z., Elsworth, D., & Wang, M. (2020). Does low-viscosity fracturing fluid always
571 create complex fractures? *Journal of Geophysical Research: Solid Earth*, *125*(9),
572 e2020JB020332.
- 573 Chen, Z., Jin, X., & Wang, M. (2018). A new thermo-mechanical coupled dem model with
574 non-spherical grains for thermally induced damage of rocks. *Journal of the Mechanics*
575 *and Physics of Solids*, *116*, 54–69.
- 576 Chen, Z., & Wang, M. (2017). Pore-scale modeling of hydromechanical coupled mechanics
577 in hydrofracturing process. *Journal of Geophysical Research: Solid Earth*, *122*(5),
578 3410–3429.
- 579 Chen, Z., & Wang, M. (2020). An improved immersed moving boundary for hydrodynamic
580 force calculation in lattice boltzmann method. *International Journal for Numerical*
581 *Methods in Engineering*, *121*(20), 4493–4508.
- 582 Cheng, S., Zhang, M., Zhang, X., Wu, B., Chen, Z., Lei, Z., & Tan, P. (2022). Numerical
583 study of hydraulic fracturing near a wellbore using dual boundary element method.
584 *International Journal of Solids and Structures*, *239*, 111479.
- 585 Cundall, P. A., & Strack, O. D. (1979). A discrete numerical model for granular assemblies.
586 *geotechnique*, *29*(1), 47–65.
- 587 Dahi-Taleghani, A., & Olson, J. E. (2011). Numerical modeling of multistranded-hydraulic-
588 fracture propagation: accounting for the interaction between induced and natural
589 fractures. *SPE journal*, *16*(03), 575–581.
- 590 De Pater, C., & Beugelsdijk, L. (2005). Experiments and numerical simulation of hydraulic
591 fracturing in naturally fractured rock. In *Alaska rocks 2005, the 40th us symposium*

- 592 *on rock mechanics (usrms)*.
- 593 Duan, K., Kwok, C. Y., Wu, W., & Jing, L. (2018). Dem modeling of hydraulic fractur-
594 ing in permeable rock: influence of viscosity, injection rate and in situ states. *Acta*
595 *Geotechnica*, *13*(5), 1187–1202.
- 596 Fazio, M., Ibemesi, P., Benson, P., Bedoya-González, D., & Sauter, M. (2021). The role
597 of rock matrix permeability in controlling hydraulic fracturing in sandstones. *Rock*
598 *Mechanics and Rock Engineering*, *54*(10), 5269–5294.
- 599 Galindo-Torres, S. (2013). A coupled discrete element lattice boltzmann method for the sim-
600 ulation of fluid–solid interaction with particles of general shapes. *Computer Methods*
601 *in Applied Mechanics and Engineering*, *265*, 107–119.
- 602 Galindo-Torres, S. A., Alonso-Marroquín, F., Wang, Y., Pedroso, D., & Castano, J. M.
603 (2009). Molecular dynamics simulation of complex particles in three dimensions and
604 the study of friction due to nonconvexity. *Physical Review E*, *79*(6), 060301.
- 605 Galindo-Torres, S. A., Pedroso, D., Williams, D., & Li, L. (2012). Breaking processes in
606 three-dimensional bonded granular materials with general shapes. *Computer Physics*
607 *Communications*, *183*(2), 266–277.
- 608 Gandossi, L., & Von Estorff, U. (2013). An overview of hydraulic fracturing and other
609 formation stimulation technologies for shale gas production. *Eur. Commisison Jt.*
610 *Res. Cent. Tech. Reports*, *26347*.
- 611 Gong, F., Zhang, L., & Wang, S. (2019). Loading rate effect of rock material with the direct
612 tensile and three brazilian disc tests. *Advances in Civil Engineering*, *2019*.
- 613 Goodfellow, S., Nasser, M., Maxwell, S., & Young, R. (2015). Hydraulic fracture energy
614 budget: Insights from the laboratory. *Geophysical Research Letters*, *42*(9), 3179–3187.
- 615 Heider, Y. (2021). A review on phase-field modeling of hydraulic fracturing. *Engineering*
616 *Fracture Mechanics*, *253*, 107881.
- 617 Huang, B., & Liu, J. (2017). Experimental investigation of the effect of bedding planes on
618 hydraulic fracturing under true triaxial stress. *Rock Mechanics and Rock Engineering*,
619 *50*(10), 2627–2643.
- 620 Kumari, W., Ranjith, P., Perera, M., Li, X., Li, L., Chen, B., ... De Silva, V. (2018).
621 Hydraulic fracturing under high temperature and pressure conditions with micro ct
622 applications: geothermal energy from hot dry rocks. *Fuel*, *230*, 138–154.
- 623 Lecampion, B. (2009). An extended finite element method for hydraulic fracture problems.
624 *Communications in Numerical Methods in Engineering*, *25*(2), 121–133.

- 625 Liu, P., Ju, Y., Gao, F., Ranjith, P. G., & Zhang, Q. (2018). Ct identification and frac-
626 tal characterization of 3-d propagation and distribution of hydrofracturing cracks in
627 low-permeability heterogeneous rocks. *Journal of Geophysical Research: Solid Earth*,
628 *123*(3), 2156–2173.
- 629 Liu, P., Ju, Y., Ranjith, P. G., Zheng, Z., Wang, L., & Wanniarachchi, A. (2016). Visual
630 representation and characterization of three-dimensional hydrofracturing cracks within
631 heterogeneous rock through 3d printing and transparent models. *International Journal*
632 *of Coal Science & Technology*, *3*(3), 284–294.
- 633 Mohammadnejad, T., & Khoei, A. (2013). An extended finite element method for hydraulic
634 fracture propagation in deformable porous media with the cohesive crack model. *Finite*
635 *Elements in Analysis and Design*, *73*, 77–95.
- 636 Morgan, S., Li, B., & Einstein, H. (2017). Effect of injection rate on hydraulic fracturing
637 of opalinus clay shale. In *51st us rock mechanics/geomechanics symposium*.
- 638 Nagaso, M., Mikada, H., & Takekawa, J. (2015). The role of fluid viscosity in hydraulic
639 fracturing in naturally fractured rock. In *Seg technical program expanded abstracts*
640 *2015* (pp. 3214–3218). Society of Exploration Geophysicists.
- 641 Noble, D., & Torczynski, J. (1998). A lattice-boltzmann method for partially saturated
642 computational cells. *International Journal of Modern Physics C*, *9*(08), 1189–1201.
- 643 Olson, J. E., & Taleghani, A. D. (2009). Modeling simultaneous growth of multiple hydraulic
644 fractures and their interaction with natural fractures. In *Spe hydraulic fracturing*
645 *technology conference*.
- 646 O’Sullivan, C., & Bray, J. D. (2004). Selecting a suitable time step for discrete element
647 simulations that use the central difference time integration scheme. *Engineering Com-*
648 *putations*.
- 649 Pan, X.-H., Xiong, Q.-Q., & Wu, Z.-J. (2018). New method for obtaining the homogeneity
650 index m of weibull distribution using peak and crack-damage strains. *International*
651 *Journal of Geomechanics*, *18*(6), 04018034.
- 652 Papachristos, E., Scholtès, L., Donzé, F., & Chareyre, B. (2017). Intensity and volumetric
653 characterizations of hydraulically driven fractures by hydro-mechanical simulations.
654 *International Journal of Rock Mechanics and Mining Sciences*, *93*, 163–178.
- 655 Peirce, A., & Detournay, E. (2009). An eulerian moving front algorithm with weak-form tip
656 asymptotics for modeling hydraulically driven fractures. *Communications in numerical*
657 *methods in engineering*, *25*(2), 185–200.

- 658 Pruess, K. (2006). Enhanced geothermal systems (egs) using co2 as working fluid—a novel
659 approach for generating renewable energy with simultaneous sequestration of carbon.
660 *Geothermics*, 35(4), 351–367.
- 661 Rahman, M., Hossain, M., & Rahman, S. (2002). A shear-dilation-based model for evalua-
662 tion of hydraulically stimulated naturally fractured reservoirs. *International Journal*
663 *for Numerical and Analytical Methods in Geomechanics*, 26(5), 469–497.
- 664 Shimizu, H., Murata, S., & Ishida, T. (2011). The distinct element analysis for hydraulic
665 fracturing in hard rock considering fluid viscosity and particle size distribution. *Inter-*
666 *national journal of rock mechanics and mining sciences*, 48(5), 712–727.
- 667 Stanchits, S., Surdi, A., Gathogo, P., Edelman, E., & Suarez-Rivera, R. (2014). Onset of hy-
668 draulic fracture initiation monitored by acoustic emission and volumetric deformation
669 measurements. *Rock Mechanics and Rock Engineering*, 47(5), 1521–1532.
- 670 Van Mier, J. G., van Vliet, M. R., & Wang, T. K. (2002). Fracture mechanisms in particle
671 composites: statistical aspects in lattice type analysis. *Mechanics of Materials*, 34(11),
672 705–724.
- 673 Wang, Y., Li, X., & Tang, C. (2016). Effect of injection rate on hydraulic fracturing
674 in naturally fractured shale formations: a numerical study. *Environmental Earth*
675 *Sciences*, 75(11), 1–16.
- 676 Wangen, M. (2011). Finite element modeling of hydraulic fracturing on a reservoir scale in
677 2d. *Journal of Petroleum Science and Engineering*, 77(3-4), 274–285.
- 678 Warpinski, N., Wolhart, S., & Wright, C. (2004). Analysis and prediction of microseismicity
679 induced by hydraulic fracturing. *Spe Journal*, 9(01), 24–33.
- 680 Warpinski, N. R., Wolhart, S., Wright, C., et al. (2001). Analysis and prediction of mi-
681 croseismicity induced by hydraulic fracturing. In *Spe annual technical conference and*
682 *exhibition*.
- 683 Wilson, Z. A., & Landis, C. M. (2016). Phase-field modeling of hydraulic fracture. *Journal*
684 *of the Mechanics and Physics of Solids*, 96, 264–290.
- 685 Yousefi, A., & Ng, T.-T. (2017). Dimensionless input parameters in discrete element model-
686 ing and assessment of scaling techniques. *Computers and Geotechnics*, 88, 164–173.
- 687 Yushi, Z., Shicheng, Z., Tong, Z., Xiang, Z., & Tiankui, G. (2016). Experimental inves-
688 tigation into hydraulic fracture network propagation in gas shales using ct scanning
689 technology. *Rock Mechanics and Rock Engineering*, 49(1), 33–45.
- 690 Zeng, Z., & Roegiers, J.-C. (2002). Experimental observation of injection rate influence on

- 691 the hydraulic fracturing behavior of a tight gas sandstone. In *Spe/isrm rock mechanics*
692 *conference*.
- 693 Zhao, X., Huang, B., & Xu, J. (2019). Experimental investigation on the characteristics of
694 fractures initiation and propagation for gas fracturing by using air as fracturing fluid
695 under true triaxial stresses. *Fuel*, *236*, 1496–1504.
- 696 Zhao, Y., Zhang, Y., Wang, C., & Liu, Q. (2022). Hydraulic fracturing characteristics and
697 evaluation of fracturing effectiveness under different anisotropic angles and injection
698 rates: an experimental investigation in absence of confining pressure. *Journal of*
699 *Natural Gas Science and Engineering*, *97*, 104343.
- 700 Zhu, W., He, X., Khirevich, S., & Patzek, T. W. (2022). Fracture sealing and its impact on
701 the percolation of subsurface fracture networks. *J. Pet. Sci. Eng.*, *218*, 111023.
- 702 Zhuang, L., Kim, K. Y., Jung, S. G., Diaz, M., & Min, K.-B. (2019). Effect of water
703 infiltration, injection rate and anisotropy on hydraulic fracturing behavior of granite.
704 *Rock Mechanics and Rock Engineering*, *52*(2), 575–589.
- 705 Zhuang, L., & Zang, A. (2021). Laboratory hydraulic fracturing experiments on crystalline
706 rock for geothermal purposes. *Earth-Science Reviews*, *216*, 103580.